AGU PUBLICATIONS

JGR

Journal of Geophysical Research: Space Physics

RESEARCH ARTICLE
10.1002/2016JA022520

Key Points:
- During high-speed stream-driven storms, the electron and proton radiation belts are directly enhanced by a single substorm
- The enhancing substorm occurs during the "strong stretching" phase of the storm caused by the superdense plasma sheet
- Proton and electron injection to 1 MeV is seen for these strong stretching phase substorms

Correspondence to:
J. E. Borovsky,
jborovsky@spacescience.org

Citation:
Borovsky, J. E., T. E. Cayton, M. H. Denton, R. D. Belian, R. A. Christensen, and J. C. Ingraham (2016), The proton and electron radiation belts at geosynchronous orbit: Statistics and behavior during high-speed stream-driven storms, *J. Geophys. Res. Space Physics, 121*, 5449–5488, doi:10.1002/2016JA022520.

Received 9 FEB 2016
Accepted 6 JUN 2016
Accepted article online 8 JUN 2016
Published online 28 JUN 2016

The proton and electron radiation belts at geosynchronous orbit: Statistics and behavior during high-speed stream-driven storms

Joseph E. Borovsky[1,2], Thomas E. Cayton[3], Michael H. Denton[1,4], Richard D. Belian[5], Roderick A. Christensen[6], and J. Charles Ingraham[6]

[1]Center for Space Plasma Physics, Space Science Institute, Boulder, Colorado, USA, [2]Climate and Space Sciences and Engineering, University of Michigan, Ann Arbor, Michigan, USA, [3]Rio Rancho, New Mexico, USA, [4]New Mexico Consortium, Los Alamos, New Mexico, USA, [5]Tesuque, New Mexico, USA, [6]Los Alamos, New Mexico, USA

Abstract The outer proton radiation belt (OPRB) and outer electron radiation belt (OERB) at geosynchronous orbit are investigated using a reanalysis of the LANL CPA (Charged Particle Analyzer) 8-satellite 2-solar cycle energetic particle data set from 1976 to 1995. Statistics of the OPRB and the OERB are calculated, including local time and solar cycle trends. The number density of the OPRB is about 10 times higher than the OERB, but the 1 MeV proton flux is about 1000 times less than the 1 MeV electron flux because the proton energy spectrum is softer than the electron spectrum. Using a collection of 94 high-speed stream-driven storms in 1976–1995, the storm time evolutions of the OPRB and OERB are studied via superposed epoch analysis. The evolution of the OERB shows the familiar sequence (1) prestorm decay of density and flux, (2) early-storm dropout of density and flux, (3) sudden recovery of density, and (4) steady storm time heating to high fluxes. The evolution of the OPRB shows a sudden enhancement of density and flux early in the storm. The absence of a proton dropout when there is an electron dropout is noted. The sudden recovery of the density of the OERB and the sudden density enhancement of the OPRB are both associated with the occurrence of a substorm during the early stage of the storm when the superdense plasma sheet produces a "strong stretching phase" of the storm. These storm time substorms are seen to inject electrons to 1 MeV and protons to beyond 1 MeV into geosynchronous orbit, directly producing a suddenly enhanced radiation belt population.

1. Introduction

Although the outer proton radiation belt has been observed by spacecraft instrumentation for five decades [e.g., *Davis and Williamson*, 1963, 1966; *Yershkovitch et al.,* 1965; *Stevens et al.,* 1970; *Spjeldvik*, 1977; *Fritz and Spjeldvik*, 1979; *Sheldon,* 1994; *Green et al.,* 2004; *Lazutin et al.,* 2007, 2012; *Tverskaya et al.,* 2008; *Forster et al.,* 2013], much less is known about its properties and dynamics than is known about the outer electron radiation belt. Modeling efforts for the outer proton radiation belt in those five decades [e.g., *Nakada and Mead*, 1965; *Spjeldvik,* 1977; *Beutier et al.,* 1995; *Bourdarie et al.,* 1997; *Boscher et al.,* 1998; *Vacaresse et al.,* 1999; *Panasyuk,* 2004; *Smolin*, 2010, 2012] have been much less sophisticated than the modeling efforts for the outer electron radiation belt. Further, the systems-science coupling of the outer electron radiation belt to other plasma populations of the magnetosphere such as the plasma sheet and ring current [*Ebihara et al.,* 2008; *Jordanova*, 2012], the outer plasmasphere [*Borovsky and Steinberg*, 2006; *Borovsky and Denton*, 2009a], the plasmaspheric drainage plume [*Borovsky et al.,* 2014], substorm injection electrons [*Friedel et al.,* 2002], and waves driven by those populations such as ULF waves [*Ozeke et al.,* 2012], chorus [*Meredith et al.,* 2002; *Summers et al.,* 2004], and electromagnetic ion cyclotron (EMIC) [*Ukhorskiy et al.,* 2010; *Lazutin et al.,* 2012] has been considered; how the outer proton radiation belt fits into the coupled system has been less well considered. Of particular relevance for the present study, the evolution of the outer electron radiation belt through high-speed stream-driven (corotating interaction region (CIR)-driven) storms has been repeatedly investigated [*Paulikas and Blake*, 1976; *Belian et al.,* 1996; *Borovsky et al.,* 1998a; *Lam,* 2004; *Miyoshi and Kataoka*, 2005; *Kataoka and Miyoshi*, 2006; *Borovsky and Denton*, 2009a, 2009b, 2010a, 2011a, 2011b; *McPherron et al.,* 2009; *Denton et al.,* 2010], but the evolution of the outer proton radiation belt has not been studied.

Mechanisms that are thought to act on the outer proton radiation belt include radial diffusion caused by magnetic and electric perturbations [e.g., *Nakada et al.,* 1965; *Cornwall*, 1972; *Beutier et al.,* 1995; *Boscher et al.,* 1998; *Vacaresse et al.,* 1999; *Panasyuk*, 2004] including substorm perturbations [*Spjeldvik*, 1977; *Smolin,* 2010],

pitch angle scattering by magnetic field curvature effects in the stretched nightside magnetic field [*Tsyganenko*, 1982; *Sergeev et al.,* 2015], pitch angle scattering and energy diffusion by plasmaspheric whistler mode hiss [*Kozyra et al.,* 1994; *Villalon and Burke*, 1994] and by ion cyclotron waves [*Søraas et al.,* 1999; *Shoji and Omura*, 2012], and charge exchange and Coulomb scattering [*Liemohn*, 1961; *Beutier et al.,* 1995; *Walt et al.,* 2001]. Potential sources for the outer proton radiation belt include solar protons [*Lazutin et al.,* 2007; *Panasyuk,* 2004; *Tverskaya et al.,* 2008] and substorm particle injections [*Vacaresse et al.,* 1999]. Finite gyroradius effects can be important for the proton radiation belt, whereas in the nominal dipole field strength of 106 nT at geosynchronous orbit (6.6 R_E) a 1 MeV ($\gamma = 1.001$) proton has a gyroradius r_g of 1370 km, whereas a 1 MeV ($\gamma = 2.96$) electron has a gyroradius of 45 km (using the formula $r_g = [(2Em)^{1/2}c/eB][1 + (E/2mc^2)]^{1/2}$ with kinetic energy E.

In this report the outer proton and electron radiation belts at geosynchronous orbit will be examined with a newly reanalyzed 8-satellite CPA data set from the years 1976–1995. The LANL CPA (Charged Particle Analyzer) instruments [*Higbie et al.,* 1978; *Baker et al.,* 1985; *Cayton et al.,* 1989] in geosynchronous orbit were predecessors to the well-utilized LANL SOPA (Synchronous Orbit Particle Analyzer) instruments [*Belian et al.,* 1992; *Cayton and Belian*, 2007] in geosynchronous orbit (1989 to present). In comparison with the SOPA instruments, the CPA instruments (1) were more sensitive, (2) had a wider energy range, and (3) did not suffer from electron contamination of the ion measurements. In this report the advantage of these three points will be taken to use the CPA data set to examine the properties of the proton radiation belt at geosynchronous orbit over two solar cycles in comparison with the electron radiation belt at geosynchronous orbit. Particular attention is paid to the behavior of the radiation belts during high-speed stream-driven geomagnetic storms.

The outer proton radiation belt at geosynchronous orbit will be surveyed and compared with the electron radiation belt. Local time and solar cycle dependencies will be examined. Using a collection of high-speed stream-driven storms in the years 1976–1995, the behavior of the outer proton radiation belt will be examined. A general absence of storm time dropouts of the proton radiation belt (when there are dropouts of the electron radiation belt) will be seen; this may have implications for the mechanisms of electron and proton loss from the magnetosphere. Sudden enhancements of the density of the proton radiation belt will be seen during storms, and these will be temporally associated with the occurrence of a substorm during the strong stretching phase of the storm. (Early in a high-speed stream-driven storm there is a "strong stretching phase" wherein the diamagnetism of the superdense plasma sheet produces a tail-like stretching of the nightside dipole that lasts for several hours [cf. *Borovsky et al.,* 1998a; *Borovsky and Denton*, 2010b].) Density enhancements of the electron radiation belt are also found to be associated with this strong stretching phase substorm. Examination of the raw count rates of the CPA instruments on multiple spacecraft finds the injection of electrons to 1 MeV and protons to beyond 1 MeV into geosynchronous orbit associated with these strong stretching phase substorms. This substorm association with the density enhancements may have implications for the seed populations of the electron and proton radiation belts.

This manuscript is organized as follows. In section 2 the geosynchronous orbit CPA data set is reviewed and the cleaning of the proton data to remove solar proton events (SPEs) is discussed. In section 3 statistical properties of the proton and electron radiation belts at geosynchronous orbit are shown, including local time dependences and solar cycle trends. In section 4 the evolution of the proton and electron radiation belts at geosynchronous orbit during high-speed stream-driven geomagnetic storms is studied with the use of superposed epoch analysis and the examination of individual events; radiation belt density dropouts and density enhancements are examined and the injection of radiation belt protons and electrons to energies of 1 MeV and above by storm time substorms is examined. In section 5.1 the timing of electron radiation belt dropout and recoveries and of proton radiation belt enhancements during the passage of corotating interaction regions is investigated. In section 5.2 the production of particles for the outer proton radiation belt and the outer electron radiation belt by storm time substorms is discussed. In section 5.3 the absence of proton radiation belt dropouts is discussed. In section 5.4 the responses of the proton radiation belt and electron radiation belt to the solar wind are analyzed. The findings of this study are summarized in section 6.

2. The CPA Data Set

The CPA (Charged Particle Analyzer) instruments [*Higbie et al.,* 1978; *Baker et al.,* 1979, 1985] were operated on eight spacecraft in geosynchronous orbit (6.6 R_E) during the years 1976–1995. Telemetry of the satellites was

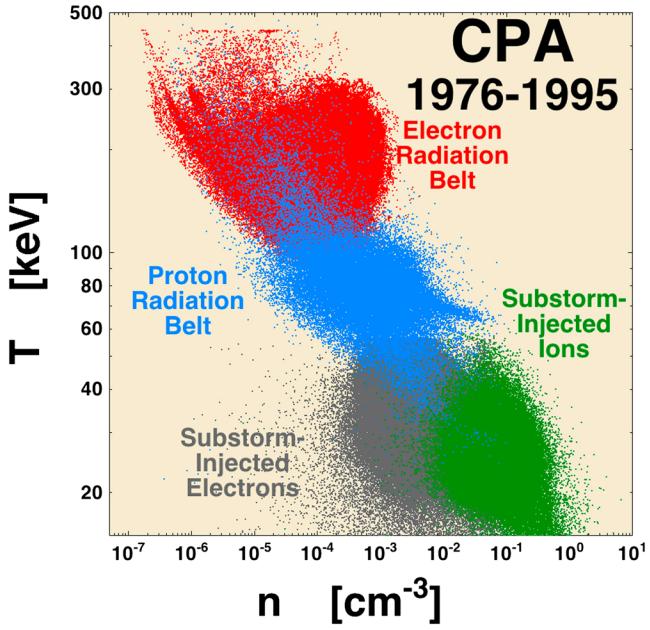

Figure 1. For the proton radiation belt (blue), the electron radiation belt (red), the population of substorm-injected ions (green), and the population of substorm-injected electrons (gray); the number density and temperature of the Maxwellian fits at geosynchronous orbit are plotted. Each point represents 30 min of measurements. All eight spacecraft for years 1976–1995 are used, and all local times are included.

intermittent, but of the 56 satellite years of measurements made, 33.4 satellite years of energetic particle measurements were collected into the CPA data set. CPA instruments contained separate ion and electron detectors, eliminating much of the electron contamination of proton measurements [*Cayton*, 2007]. Protons with energies of 50 keV–250 MeV were analyzed in 26 energy channels; electrons with energies of 30 keV–2 MeV were analyzed in 12 energy channels.

A recent reanalysis of the CPA proton and electron data sets was performed, and the technical details of that process will be published separately. The reanalysis involved reinvestigation of laboratory fabrication, calibration, and assembly records and involved modernized Monte Carlo simulations of the behavior of particles in revised models of the CPA instruments. Satellite-to-satellite systematic errors were corrected. The data reanalysis yielded improved fluxes and yielded improved two-Maxwellian (two-exponential) energy distribution fits to the measured proton and electron count rates [*Cayton et al.,* 1989]. Each Maxwellian fit has two parameters, a number density n and a temperature T. The number density n is a measure of the number of particles in that distribution, and the temperature T is a measure of the hardness of the energy spectra of that distribution.

The analysis in this report is based on 30 min resolution averages of the CPA proton and electron data products.

The CPA proton data set has been cleaned to remove cataloged solar proton events (SPEs) using the NOAA Space Environment Services Center Solar Proton Events list (at ftp://ftp.swpc.noaa.gov/pub/indices/SPE.txt) and the more complete *Kurt et al.* [2004] SPE list. Those two catalogs provide event start times and times of peak fluxes but do not contain event termination times. To get termination times, the energetic proton measurements from the Goddard Medium Energy Experiment [*McGuire et al.,* 1986] on board the IMP-8 spacecraft in the solar wind were utilized, paying specific attention to the 10 MeV and 1 MeV proton fluxes in the solar wind at Earth. Cleaning for SPEs removed about 7.2% of the proton measurements from the CPA data set, chiefly during the solar maxima years 1981, 1982, 1989, and 1991 [cf. *Kurt et al.*, 2004, Figure 2f]. Note that the NOAA and *Kurt et al.*'s [2004] SPE lists are incomplete and that there are SPE events that have not been removed from the CPA proton data set.

In Figure 1 the n and T values are plotted for the entire 20 year, 8-spacecraft CPA proton and electron data set. The hotter and the cooler distributions for the electrons and the protons are plotted in four different colors. Examining the temporal behaviors of the hotter and the cooler distributions for both the electrons and the protons [cf. *Cayton et al.,* 1989; *Denton et al.,* 2010; *Denton and Borovsky*, 2012], the lower temperature distributions are identified as substorm-injected electrons and protons and the higher-temperature distributions are identified as the electron radiation belt and the proton radiation belt [see also *Pierrard and Lemaire*, 1996]. Note in Figure 1 that for both the radiation belts and the substorm-injected particles, the proton density is on average higher than the electron density. Of interest in the present study are the proton radiation belt (blue points) and the electron radiation belt (red points).

Note in the distribution of blue proton radiation belt points in Figure 1 that there is a halo of higher-temperature (T greater than about 100 keV) points; these higher-temperature points are mostly owed to

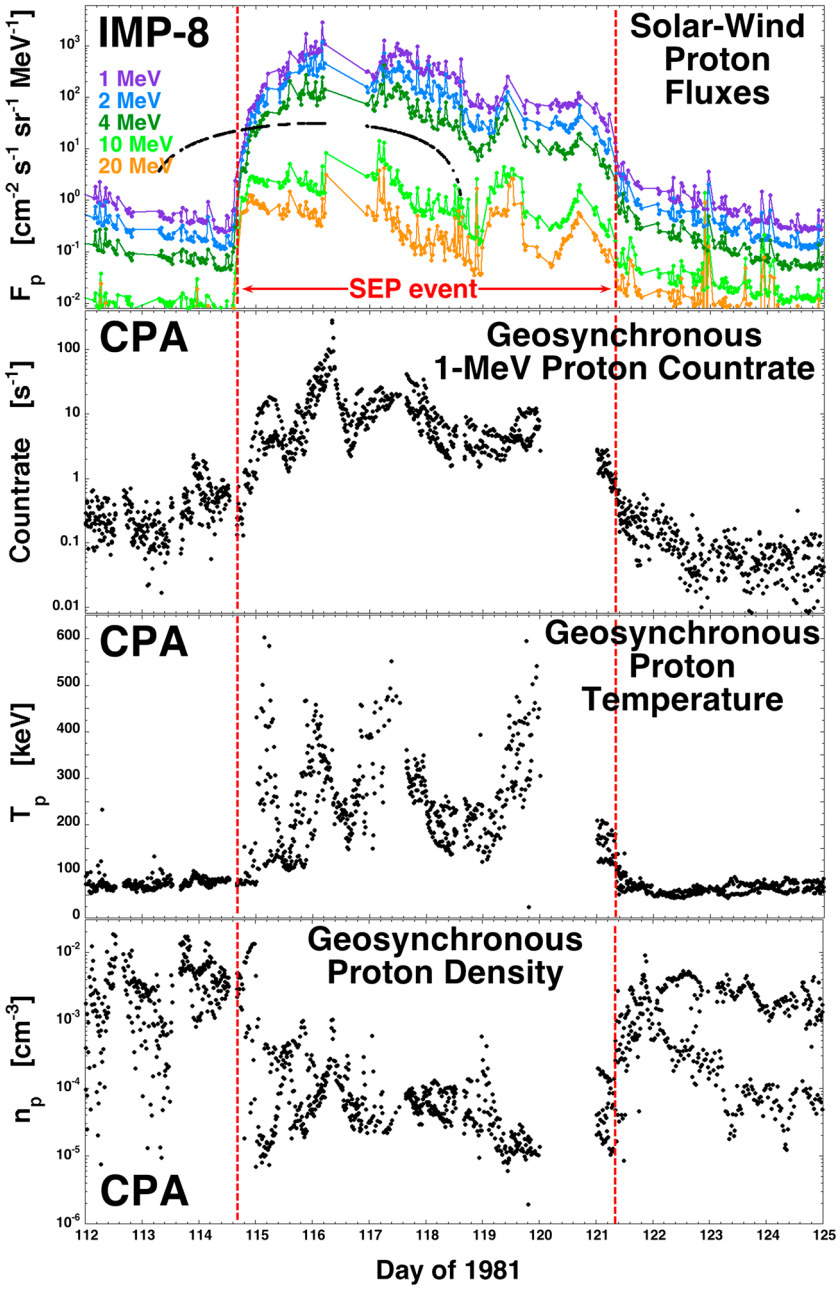

Figure 2. For a solar proton event (SPE) commencing on April 24 (Day 114) 1981, (first panel) the IMP-8 energetic proton fluxes in the solar wind and the (second panel) 1 MeV proton flux, (third panel) proton radiation belt temperature, and (fourth panel) proton radiation belt number density as measured by four geosynchronous spacecraft (1976-059, 1977-007, 1979-053, and 1981-025). All local times are included.

protons from solar proton events (SPEs) events diffusing into the magnetosphere. In Figure 2 the effect of an SPE on the CPA proton measurements is examined. The SPE of Figure 2, with an onset on 24 April 1981, was examined by *Reames et al.* [1990] using ISEE 3 solar wind energetic proton measurements; this particular SPE is not on the NOAA SPE list but is on the *Kurt et al.* [2004] SPE list. In Figure 2 (first panel) the differential fluxes of energetic protons as measured by the Goddard Medium Energy Experiment [*McGuire et al.,* 1986] on board the IMP-8 spacecraft in the solar wind are plotted as functions of time for 13 days in 1981; various energies from 1 to 20 MeV are plotted in various colors. The GSE X position of IMP-8 is plotted as the black points in Figure 2 (first panel) when $X > 0$; IMP-8 was in a 12.4 day quasicircular orbit with a radius of 30–40 R_E. When $X > 0$, IMP-8 was out in front of the Earth in the solar wind and magnetosheath, and IMP-8 is in the solar

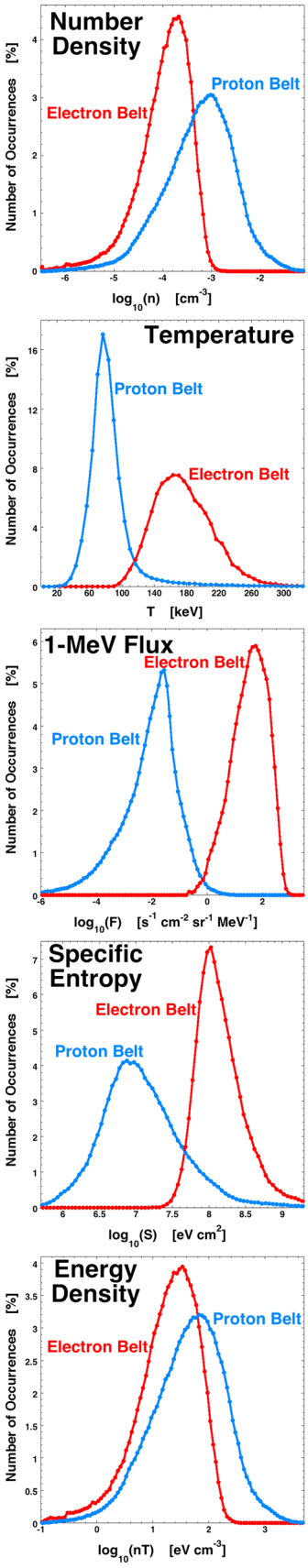

wind or the magnetosheath in all portions of its orbit except the $-X$ extrema when it is passing through the magnetotail. In Figure 2 the $-X$ extrema occurred on day 121; the Magnetic Field Experiment on IMP-8 [cf. *Paularena and King*, 1999] indicates magnetotail-like magnetic field orientations from day 121.33 to day 122.95. The onset time of the SPE as measured by the IMP-8 spacecraft in the solar wind is denoted as the first vertical red dashed line in Figure 2. At the marked SPE onset time (16:20 UT on 24 April 1981) the location of IMP-8 was GSE $(X, Y, Z) = (22.6, -25.4, -12.2)\, R_E$. The termination of the SPE as determined by the proton fluxes on IMP-8 (probably in the magnetotail at that time) is denoted by the second vertical red dashed line. In Figure 2 (second panel) the raw count rates in the 1–1.3 MeV CPA proton channel onboard four geosynchronous spacecraft (1976-059, 1977-007, 1979-053, and 1981-025) are plotted for the 13 days. The high proton count rates at geosynchronous orbit in Figure 2 (second panel) temporally correspond to the high fluxes of energetic protons in the solar wind in Figure 2 (first panel), with a time lag of about 5–6 h from the solar wind to geosynchronous orbit. In Figure 2 (third panel) the temperature T_p of the proton radiation belt is plotted for the CPA measurements on the four geosynchronous spacecraft. In Figure 2 (third panel) note the temperatures prior to the onset of the SPE and after the termination of the SPE: these are the typical temperatures for the proton radiation belt at geosynchronous orbit. During the SPE (between the two vertical dashed lines) the hot-Maxwellian proton temperature at geosynchronous orbit is greatly elevated (e.g., the blue halo points in Figure 1). In Figure 2 (fourth panel) the number density n_p of the hot-Maxwellian fit to the protons is plotted for the four geosynchronous spacecraft; during the SPE the fit is dominated by the very hard spectrum SPE protons and the density is depressed. One way to eliminate all SPEs from the CPA data set would be to eliminate all data where T_p is greater than or equal to about 150 keV—for fear of overcleaning that is not done in the present study.

Examination of the CPA electron count rates and density and temperature fits indicates that contamination of the electron radiation belt measurements at geosynchronous orbit by CPA are not strongly affected by solar proton events.

3. Statistics of the Proton and Electron Radiation Belts at Geosynchronous Orbit

In Figure 3 the occurrence distributions of five radiation belt parameters for protons and electrons at geosynchronous

Figure 3. For the 1976–1995 CPA proton and electron data set, the occurrence distributions of the (first panel) radiation belt number densities, (second panel) temperatures, (third panel) 1 MeV flux, (fourth panel) specific entropy, and (fifth panel) energy density are plotted in blue for protons and in red for electrons. All local times are included.

Table 1. Properties of the Proton and Electron Radiation Belts at Geosynchronous Orbit

	Electron Belt Mean Value	Electron Belt Median Value	Proton Belt Mean Value	Proton Belt Median Value	
n	1.7×10^{-4} cm^{-3}	1.3×10^{-4} cm^{-3}	1.7×10^{-3} cm^{-3}	6.3×10^{-4} cm^{-3}	number density
T	176 keV	172 keV	85 keV	79 keV	temperature
F	78 cm^{-2}s^{-1}sr^{-1}MeV^{-1}	38 cm^{-2}s^{-1}sr^{-1}MeV^{-1}	0.058 cm^{-2}s^{-1}sr^{-1}MeV^{-1}	0.012 cm^{-2}s^{-1}sr^{-1}MeV^{-1}	1 MeV flux
S	3.0×10^{8} cm^{2} eV	1.3×10^{8} cm^{2} eV	4.2×10^{7} cm^{2} eV	1.1×10^{7} cm^{2} eV	specific entropy
nT	33 eV cm^{-3}	32 eV cm^{-3}	116 eV cm^{-3}	49 eV cm^{-3}	energy density
P	$<3.5\times10^{-3}$ nPa	$<3.4\times10^{-3}$ nPa	1.2×10^{-2} nPa	5.2×10^{-3} nPa	kinetic pressure

orbit are plotted for the 1976–1995 CPA data set: protons in blue and electrons in red. The mean and median values of the five parameters for the proton radiation belt and electron radiation belt are collected in Table 1. In Figure 3 (first panel) the occurrence distributions of the base 10 logarithms of the number densities are plotted; note in this panel that the number of radiation belt protons at geosynchronous orbit is an order of magnitude greater than the number of radiation belt electrons (see also Table 1 and Figure 1). In Figure 3 (second panel) the distributions of the temperatures of the proton and electron radiation belts are plotted: the electron radiation belt is hotter (has a harder spectrum) than the proton radiation belt. In Figure 3 (third panel) the occurrence distributions of the base 10 logarithm of the 1 MeV differential fluxes of protons and of electrons are plotted. The flux of 1 MeV electrons at geosynchronous orbit is about 1000 times greater than the flux of 1 MeV protons at geosynchronous orbit despite the number density of protons being 10 times larger. This larger electron flux is because (1) the electron spectrum is harder and (2) the low-mass electrons are more mobile (a 1 MeV electron has a speed of 2.82×10^{10} cm/s, while a 1 MeV proton has a speed of 1.39×10^{9} cm/s—more than an order of magnitude higher. In Figure 3 (fourth panel) the occurrence distributions of the base 10 logarithm of the specific entropy S of the radiation belt protons and of the radiation belt electrons are plotted. The specific entropy S is the number density of adiabatic invariants per unit magnetic flux [*Borovsky and Cayton*, 2011]: for the protons the standard expression $S_p = T_p/n_p^{2/3}$ is used and for the electrons the relativistic expression [*Borovsky and Cayton*, 2011, equation (7)] $S_e \approx T_e(1+(T_e/137.9)^{1.275})^{1/1.275} n_e^{-2/3}$ is used. At geosynchronous orbit the specific entropy of the electron radiation belt is typically an order of magnitude greater than the specific entropy of the proton radiation belt. In Figure 3 (fifth panel) the occurrence distributions of the base 10 logarithms of the energy density nT (in eV/cm^3) of the proton and electron radiation belts at geosynchronous orbit are plotted. The proton radiation belt energy density is on average higher than the electron radiation belt energy density at geosynchronous orbit. Mean and median values appear in Table 1. These radiation belt energy densities can be compared with the energy density of the ion plasma sheet, which has the greatest energy density and particle pressure at geosynchronous orbit; for typical ion plasma sheet parameters of $n \sim 1$ cm^{-3} and $T \sim 10$ keV [cf. *Borovsky et al.*, 1998b, Figure 1] the energy density of the ion plasma sheet is nT $\sim 10^4$ eV/cm^3, about 2 orders of magnitude greater than the energy density of the proton radiation belt. For protons, the kinetic pressure (in units of nPa) of the proton radiation belt can be obtained by multiplying the energy density by 1.07×10^{-4}; owing to relativistic effects multiplying, the energy density of the electron radiation belt by 1.07×10^{-4} yields a slight overestimate of the electron radiation belt pressure. Mean and median pressure values appear in Table 1.

The local time dependence of radiation belt parameters at geosynchronous orbit is investigated in Figure 4, with proton radiation belt parameters plotted in blue and electron radiation belt parameters plotted in red. Each point in Figure 4 represents a logarithmic average of all of the data in the 8-satellite CPA data set in that hour of local time. (The logarithmic average of a quantity Q is 10^x, where $x = <\log_{10}(Q)>$.) In Figure 4 (first panel) the 1 MeV particle flux is plotted, with the proton flux multiplied by a factor of 1000. Black horizontal dashed lines are drawn to guide the eye. The vertical axis is logarithmic; the dayside to nightside proton flux varies by almost 1 order of magnitude in Figure 4 (first panel). The peak of the electron flux is located slightly dawnward of local noon; this prenoon local time maximum of the 1 MeV flux is familiar for the electron radiation belt as seen by the multisatellite SOPA data set [cf. *Denton et al.*, 2010, Figure 3] and may be related to a maximum in the geosynchronous magnetic field strength just dawnward of local noon [cf. *Borovsky and Denton*, 2010b, Figure 6). In Figure 4 (first panel) the 1 MeV proton flux does not show this dawnward shift; the proton flux maximum is near local noon. It is well known that this dayside peak in the flux (and the density and the temperature) is caused by the conservation of the first adiabatic invariant causing orbiting energetic particles to move further out on the dayside than on the nightside in the distorted

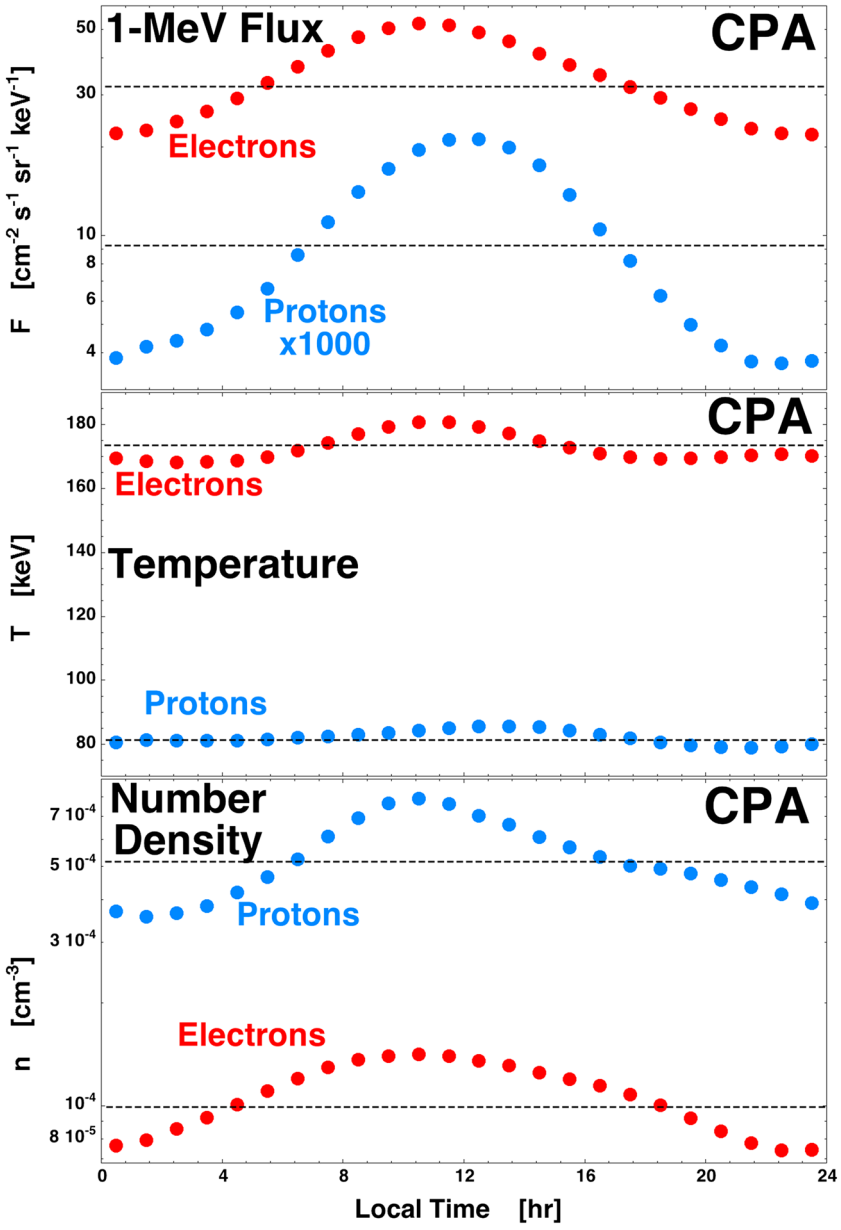

Figure 4. For the 1976–1995 CPA data set at geosynchronous orbit, the local time dependences of the (first panel) 1 MeV proton and electron flux, (second panel) proton radiation belt and electron radiation belt temperatures, and (third panel) proton radiation belt and electron radiation belt number densities are plotted. Each point represents a logarithmic average of all of the data in the 8-satellite CPA data set in that hour of local time. Note that the vertical axes for *F* and for *n* are logarithmic.

magnetosphere, leading to a dayside geosynchronous spacecraft sampling deeper into the radiation belt than does a nightside geosynchronous spacecraft [e.g., *Roederer*, 1967; *Denton et al.,* 2010]. In Figure 4 (second panel) the local time dependence of the radiation belt temperatures is plotted. As can be seen the temperature of the electron radiation belt (red) is maximum dawnward of local noon [see also *Denton et al.*, 2010, Figure 3]. For the electron radiation belt the dayside increase in temperature over the nightside temperature is about a 10% effect. The temperature of the proton radiation belt (blue) shows a very slight maximum in the vicinity of local noon, a less than 10% effect. In Figure 4 (third panel) the number density of the proton radiation belt and the electron radiation belt is plotted as a function of local time. Both the protons and the electrons show a density maximum just dawnward of local noon and show minima at local midnight; this pattern for the electron radiation belt at geosynchronous orbit is familiar [e.g., *Denton et al.*, 2010, Figure 3].

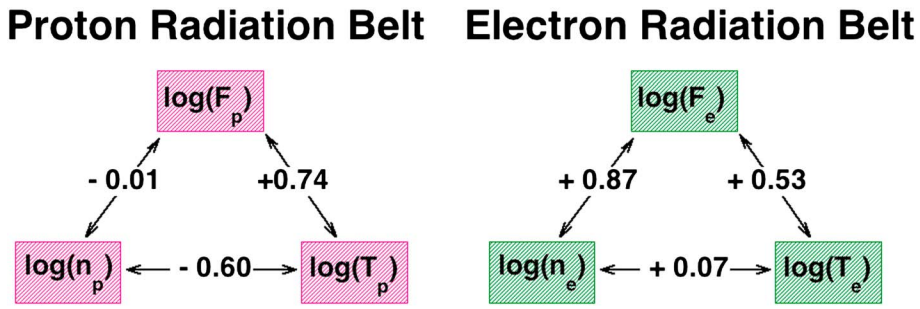

Figure 5. Pearson linear correlation coefficients between 1 MeV fluxes and the parameters of the high-Maxwellian fits for (left) the CPA protons and (right) the CPA electrons.

The Pearson linear correlation coefficients between the number density, the temperature, and the 1 MeV particle flux are displayed in Figure 5 for the proton radiation belt (left) and for the electron radiation belt (right). For the proton radiation belt the correlation between the logarithm of the 1 MeV proton flux and the logarithm of the temperature is 0.74, whereas the correlation between the logarithm of the 1 MeV proton flux and the logarithm of the number density is only −0.01; this indicates that variations in the 1 MeV proton flux are strongly related to variations in the temperature of the proton radiation belt. On the contrary in Figure 5 (right) the 1 MeV electron flux is more strongly correlated (0.87) with the number density of the electron radiation belt than it is with the temperature of the electron radiation belt (0.53); this indicates that variations in the 1 MeV electron flux are more controlled by variations in the number density of the radiation belt than they are by its temperature.

The strong temperature dependence of the 1 MeV flux for the proton radiation belt (Figure 5) may be because 1 MeV is further out on the tail of the energy distribution of the protons than it is on the energy distribution of the electrons, and the flux out on the tail of a distribution is very sensitive to the temperature of the distribution. This is demonstrated in Figure 6, where the differential flux at 1 MeV is plotted as a function of the temperature of a Maxwellian (exponential) distribution. At low temperature the flux at 1 MeV is low; as the temperature increases the flux rises rapidly with increasing temperature until a maximum of the 1 MeV flux is reached. Heating beyond this point actually lowers the flux at 1 MeV. As noted in Table 1, the median temperature of the proton radiation belt at geosynchronous orbit is 79 keV and the median temperature of the electron radiation belt at geosynchronous orbit is 172 keV. The blue region of the curve in Figure 6 is the 1 MeV flux as the temperature goes from 74 keV to 84 keV; the red region of the curve is the 1 MeV flux as the temperature goes from 167 keV to 177 keV. For the 10 keV change in the temperature around 79 keV the proton flux increases by a multiplicative factor of 3.90, whereas for a 10 keV change in the temperature around 172 keV the electron flux increase is only by a multiplicative factor of 1.24. Another way to look at this is that for the black curve in Figure 6, the derivative $d\log_{10}(F)/dT = 6.0\times10^{-2}\,\mathrm{keV}^{-1}$ at $T = 79$ keV and $d\log_{10}(F)/dT = 9.7\times10^{-3}\,\mathrm{keV}^{-1}$

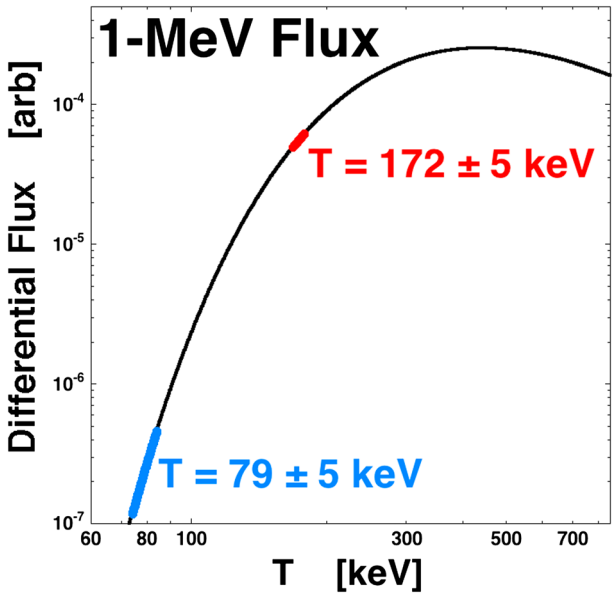

Figure 6. For a Maxwellian distribution, the 1 MeV differential flux is plotted as a function of the distribution temperature. The red part of the curve represents the flux-temperature behavior for typical electron radiation belt values and the blue part of the curve represents the flux-temperature behavior for typical proton radiation belt values.

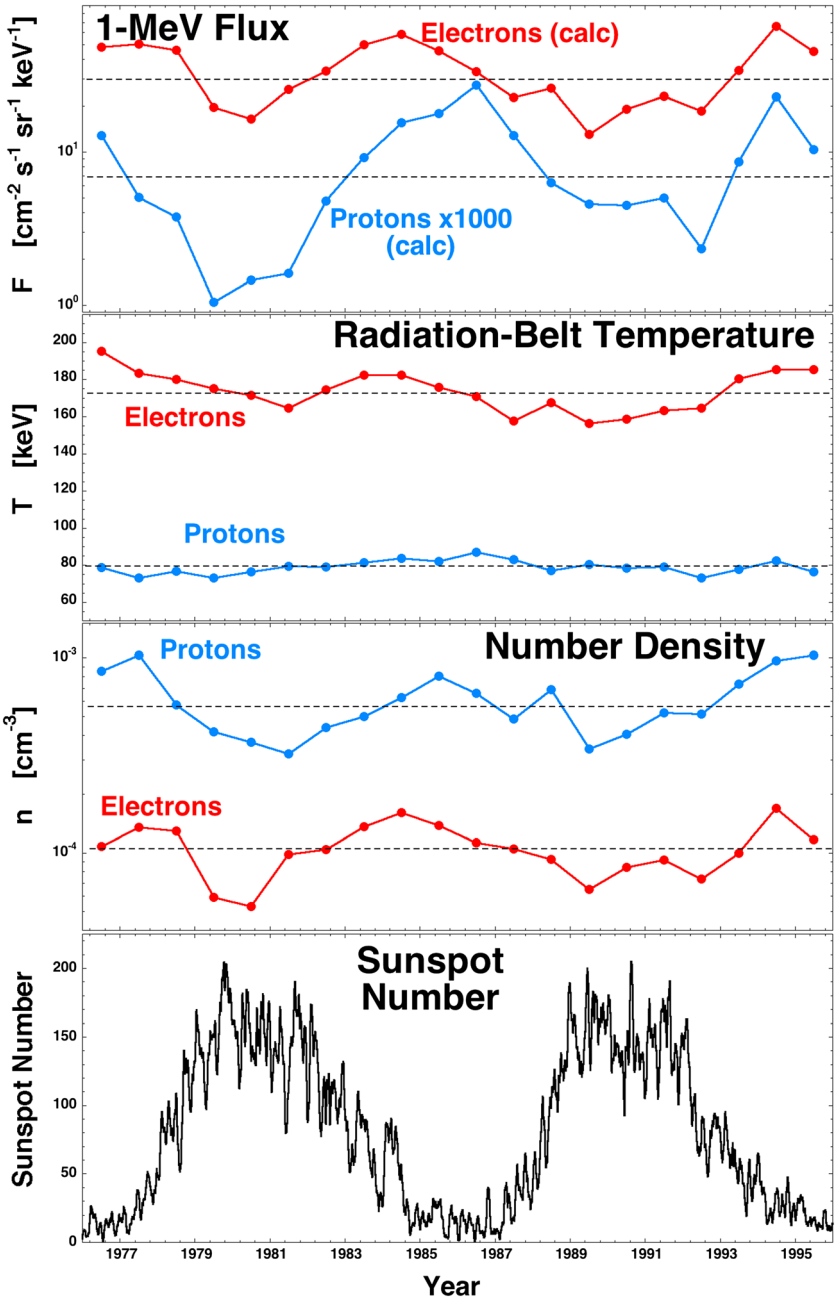

Figure 7. For the 1976–1995 CPA data set, yearly averages (first panel) of the 1 MeV proton and electron flux, (second panel) of the temperatures of the proton and electron radiation belts, and (third panel) of the number densities of the proton and electron radiation belts: each point plotted represents a logarithmic average of all of the data in the 8-satellite CPA data set for that calendar year. In Figure 7 (third panel) the monthly sunspot number is plotted.

at $T = 172$ keV, a factor of 6.2 higher at the proton temperature than it is at the electron temperature. Power law fits to the blue and red regions of the curve yield $F \propto T^{10.9}$ at 79 keV and $F \propto T^{3.8}$ at 172 keV.

In Figure 7 the properties of the proton radiation belt (blue) and the electron radiation belt (red) are examined through two solar cycles. In Figure 7 (first to third panels) each point plotted represents a logarithmic average of all of the data in the 8-satellite CPA data set for that calendar year. In Figure 7 (fourth panel) the monthly sunspot number is plotted as a function of time for the years 1976–1995; three solar minima and two solar maxima are contained in this time period. In Figure 7 (first panel) the 1 MeV differential flux of electrons (red) and protons (blue) is plotted on a logarithmic vertical axis. The electron flux in Figure 7

Table 2. Onset Times for the 95 High-Speed Stream-Driven Geomagnetic Storms in 1976–1995

Storm Number	Year	Day of Year	Onset Time (UT)
1	1976	38	10.5
2	1976	58	13.5
3	1976	65	22.5
4	1976	236	7.5
5	1976	289	7.5
6	1977	67	22.5
7	1977	262	10.5
8	1978	29	4.5
9	1978	56	19.5
10	1978	85	1.5
11	1980	132	10.5
12	1981	84	4.5
13	1982	21	16.5
14	1982	48	7.5
15	1982	146	13.5
16	1983	87	4.5
17	1983	113	22.5
18	1983	141	13.5
19	1983	168	16.5
20	1984	155	13.5
21	1984	195	4.5
22	1984	213	22.5
23	1984	240	13.5
24	1984	266	19.5
25	1984	280	22.5
26	1984	292	4.5
27	1985	8	19.5
28	1985	36	7.5
29	1985	64	4.5
30	1985	157	13.5
31	1985	185	13.5
32	1985	212	7.5
33	1985	224	19.5
34	1985	262	10.5
35	1985	278	4.5
36	1985	306	13.5
37	1986	51	16.5
38	1986	80	13.5
39	1986	232	19.5
40	1986	254	19.5
41	1986	266	4.5
42	1986	286	16.5
43	1987	51	4.5
44	1987	196	13.5
45	1987	224	22.5
46	1987	253	13.5
47	1987	286	13.5
48	1987	300	1.5
49	1987	327	7.5
50	1987	349	16.5
51	1989	20	13.5
52	1989	115	13.5
53	1989	143	13.5
54	1990	331	1.5
55	1991	226	19.5
56	1991	242	13.5
57	1991	350	13.5
58	1992	246	10.5
59	1992	261	1.5
60	1992	272	19.5

(first panel) shows the familiar maxima during the declining phases of the solar cycle [cf. *Denton et al.*, 2010, Figure 4], with the declining phase being well known for the presence of high-speed stream-driven storms [*Richardson et al.,* 2001]. The proton flux (multiplied by a factor of 1000) plotted in Figure 7 (first panel) exhibits minima at solar maxima and exhibits maxima at solar minima. Note that the proton fluxes are susceptible to SPEs that were not cleaned out of the CPA data set, with higher-than-average fluxes occurring during SPEs (cf. Figure 2); SPEs tend to occur more frequently during solar maximum so the true minima of the proton radiation belt fluxes during solar maxima may be even lower than the values plotted in Figure 7. In Figure 7 (second panel) the temperatures of the proton radiation belt and the electron radiation belt are plotted. The electron radiation belt shows slight temperature maxima during the declining phases of the solar cycles [cf. *Denton et al.*, 2010, Figure 4]; no clear solar cycle dependence is seen for the temperature of the proton radiation belt. In Figure 7 (third panel) the number densities of the proton radiation belt and the electron radiation belt are plotted. The electron radiation belt density and the proton radiation belt density both show minima at solar maxima and maxima at solar minima.

4. The Proton and Electron Radiation Belts During High-Speed Stream-Driven Geomagnetic Storms

To study high-speed stream-driven storms in the CPA era (1975–1995), a collection of 94 high-speed stream-driven storms in the years 1976–1995 is utilized (cf. Table 2). In the modern era with the availability of quality solar wind measurements, the authors have identified high-speed stream-driven storms by [e.g., *Denton and Borovsky*, 2008; *Borovsky and Denton,* 2010b,

Table 2. (continued)

Storm Number	Year	Day of Year	Onset Time (UT)
61	1992	300	19.5
62	1992	342	13.5
63	1993	227	15.5
64	1993	282	3.5
65	1993	307	19.5
66	1994	11	12.5
67	1994	26	5.5
68	1994	35	14.5
69	1994	65	19.5
70	1994	92	1.5
71	1994	121	6.5
72	1994	148	11.5
73	1994	195	10.5
74	1994	275	16.5
75	1994	295	11.5
76	1994	302	4.5
77	1994	340	6.5
78	1995	29	4.5
79	1995	42	6.5
80	1995	57	5.5
81	1995	68	8.5
82	1995	85	8.5
83	1995	96	22.5
84	1995	122	3.5
85	1995	143	19.5
86	1995	150	3.5
87	1995	170	7.5
88	1995	176	14.5
89	1995	197	13.5
90	1995	220	0.5
91	1995	225	23.5
92	1995	248	10.5
93	1995	308	13.5
94	1995	358	8.5

2013] (1) identifying corotating interaction regions (CIRs) in the solar wind data, (2) looking for long-lived high-speed streams in the solar wind data that follow the CIRs, and (3) looking at the *Kp* index to ensure that a storm occurred. Then (4) the magnetic field, proton temperature, and electron strahl structure of the solar wind data are examined to ensure that the CIR is not dominated by a magnetic cloud. Magnetic clouds are usually ejected from the magnetic sector reversals of helmet streamers [*Foullon et al.,* 2011] or from the double sector reversals of pseudostreamers [*Liu*, 2007], both of which appear at 1 AU on the leading edges of CIRs; if a magnetic cloud is prevalent in the CIR, the event is rejected as a storm of "mixed origin." Unfortunately, prior to 1995 solar wind measurements are sparse. In the OMNI2 multisatellite data base [*King and Papitashvili*, 2005] for 1976–1994, solar wind velocity measurements are only available 55% of the time. In the CPA era from 1976 to 1995, years with good solar wind data coverage are 1976 through mid-1978 with the IMP-7 and IMP-8 spacecraft, mid-1978 through mid-1982 with the ISEE-3 spacecraft, and 1995 onward with the Wind spacecraft. Particularly, poor coverage occurs in the years late 1982 through 1994 where the IMP-8 spacecraft provided solar wind data about 40% of the time with a few-days-on/few-days-off pattern of coverage.

To identify high-speed stream-driven storms in the eras of poor solar wind data coverage, 27 day repeating patterns of high *Kp* are sought, particularly temporal patterns wherein *Kp* starts low, then rises rapidly, and then stays high for a few days [cf. *Forster et al.,* 2013]. After identifying such a repeating *Kp* pattern, the available solar wind data are checked to ensure that there is slow wind in the low-*Kp* interval and that there is high-speed wind in the high *Kp* interval; the *Xu and Borovsky* [2015] plasma identification scheme is applied to the available solar wind measurements to ensure that the solar wind during the *Kp* storm is of coronal hole origin. If not, the event is rejected. The available solar wind data are examined to look for anomalously low solar wind proton temperatures and/or out-of-ecliptic IMF orientations, both of which are indicators of magnetic clouds [*Gosling et al.,* 1973; *Burlaga et al.,* 1981; *Borovsky*, 2010a]. If a cloud is prevalent, the event is rejected. Following this method, 62 high-speed stream-driven storms were identified in 1976–1992. The onset time of each storm is taken to be the middle of the first 3 h period when the 3 h resolution *Kp* index reaches a level of 4 or higher. The *Kp* index is a very good measure of the strength of magnetospheric convection [*Thomsen*, 2004]; it can be said that the onset time is taken to be the time at which magnetospheric convection reaches storm levels. These onset times are listed in Table 2.

To this list of 62 newly identified storms, 32 storms in 1993–1995 that were identified for prior high-speed stream-driven storm studies [e.g., *Borovsky and Denton*, 2010b] are added for a total of 94 storms in 1976–1995. (These are from a collection of 70 high-speed stream-driven storms in 1993–2005.) The onset times of the 32 added storms are the time at which MBI (Midnight Boundary Index [*Gussenhoven et al.,* 1983]) crosses

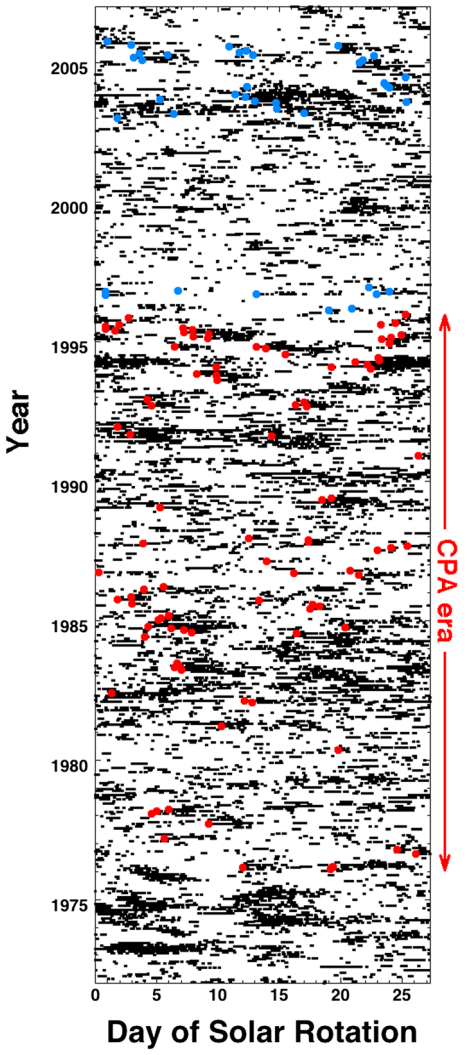

Figure 8. A day of solar rotation (horizontal) versus time (vertical) plot is made. The black points are times when the *Kp* index is 4 or greater. The red points are the onset times of the 94 high-speed stream-driven storms of Table 1 (1976–1995). The blue points (plus the red points in 1993–1995) are the onset times of 70 high-speed stream-driven storms utilized for previous radiation belt studies.

through the value 60.7° as geomagnetic activity increases; this is equivalent to *Kp* reaching 3.7. These onset times are listed in Table 2. The accuracy of the *Kp*-based storm onset trigger time is about 3 h in the 1976–1992 storms; the accuracy of the MBI-based storm onset trigger time is about 30 min for the 1993–1995 storms.

4.1. Superposed Averages Triggering on Storm Onset

In Figure 8 the trigger times of the 94 storms (see Table 2) are examined in a solar rotation versus time plot. Here time is broken into 27.27 daylong intervals, one interval for each rotation of the sun. The data are then plotted as the day during the 27.27 daylong interval (horizontal) versus the fractional year of the interval (vertical). Times when $Kp \geq 4$ are plotted as small black points; 27 day repeating storms appear as the vertical clusters of black points on the plot. Several of these storm groups can be seen in 1973–1974, in 1983–1985, in 1993–1996, and in 2003–2004, which are during four declining phases of the solar cycle. The collection of 94 storm onsets in the CPA era is plotted as the large red dots. Storms in the 70 storm collection after 1995 are plotted as the large blue dots. Storm triggers that are repeating every ~27 days can be seen in 1977, 1984, 1994, and 2003–2005.

In Figure 9 superposed epoch averaging is used to compare the solar wind speed, the solar wind density, the *AE* index, and the *Kp* index for the new collection of 62 storms in 1976–1992 with the collection of 70 storms in 1993–2005 that have been used in previous studies of high-speed stream-driven storms [e.g., *Borovsky and Denton*, 2010b]. In Figure 9 (fourth panel) the superposed average of the *Kp* index is plotted for the two sets of storms. The vertical dashed line indicates the onset times of the storms in each collection. The horizontal dashed line marks the average value of *Kp*, which is 2.3. Note prior to the storm onset that the *Kp* index is below average: this is because most high-speed stream-driven storms are preceded by a "calm before the storm" [*Borovsky and Steinberg*, 2006; *Borovsky and Denton*, 2013] wherein geomagnetic activity is unusually low. In Figure 9 (third panel) the superposed average of the *AE* index is plotted for the two sets of storms, triggered on storm onset. The temporal profile of the superposed average of *AE* mirrors the temporal profile of *Kp*. In Figure 9 (first panel) the superposed average of the solar wind speed is plotted for the two sets of storms. Note that the rise times of the speed are systematically different in the two sets, probably owing to the inaccuracy of the trigger times in the 1976–1992 storms. Note also that the superposed average of v_{sw} is noisier for the 1976–1992 storms owing to the scarcity of solar wind data during that era. In Figure 9 (first panel) the characteristic slow wind followed by fast wind pattern is seen. In Figure 9 (second panel) superposed

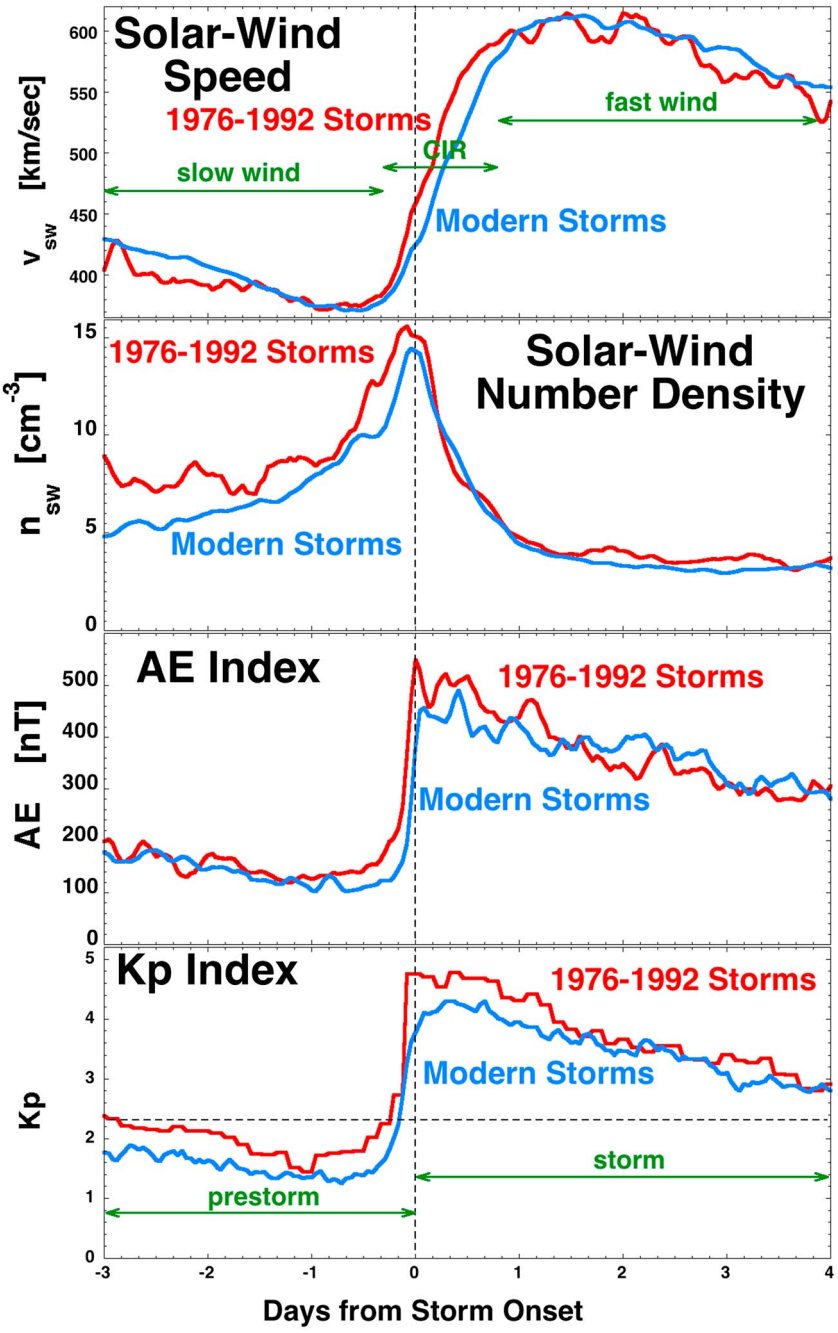

Figure 9. Using superposed epoch averaging, the set of newly collected high-speed stream-driven storms in 1976–1992 are compared with the set of 1993–2005 "modern" high-speed stream-driven storms utilized in previous studies. (first panel) The superposed average of the solar wind speed v_{sw} is plotted, (second panel) the superposed average of the solar wind number density n_{sw} is plotted, (third panel) the superposed average of the *AE* index is plotted, and (fourth panel) the superposed average of the *Kp* index is plotted.

averages of the solar wind number density are plotted for the two sets of storms. Prior to the storm the superposed average of the density of the streamer belt plasma is slightly higher than the density of the coronal hole plasma during the storm; this is caused by the presence of noncompressive density enhancements in the solar wind [*Gosling et al.,* 1981; *Borrini et al.,* 1981] likely to be sector-reversal-region plasma [*Xu and Borovsky*, 2015]. Near the time of storm onset the number density is particularly high owing to the compression of the solar wind in the corotating interaction region [*Gosling et al.,* 1978; *Richter and Luttrell*, 1986; *Borovsky and Denton*, 2010c].

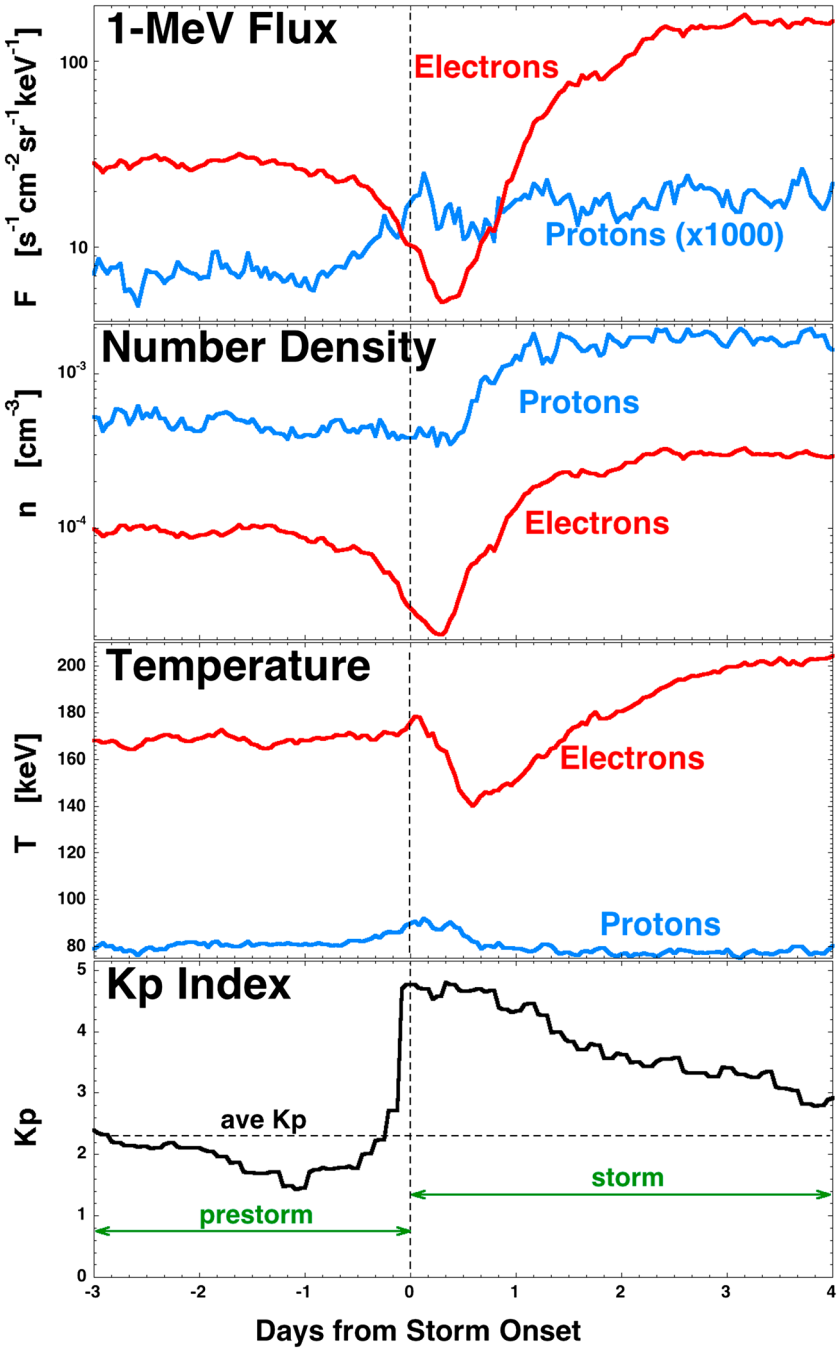

Figure 10. Using the onset times of the 94 high-speed stream-driven storms of 1976–1995 (see Table 2) for the zero epoch, (first panel) superposed averages of the CPA 1 MeV flux of protons and electrons, (second panel) superposed averages of the proton and electron radiation belt number densities, (third panel) superposed averages of the proton and electron radiation belt temperatures, and (fourth panel) superposed average of *Kp* are plotted for the 94 storms. For the CPA geosynchronous orbit measurements, all local times are included. In Figure 10 (first to third panels) the superposed averages are superposed logarithmic averages.

In Figure 10 the evolution of the proton radiation belt and the electron radiation belt is examined during high-speed stream-driven storms using CPA measurements and the 94 storms of 1976–1995. In Figure 10 (fourth panel) the superposed average of the *Kp* index is plotted, with the vertical dashed line representing storm onset as determined by *Kp*. In Figure 10 (first panel) the superposed logarithmic averages of the 1 MeV flux of electrons (red) and protons (blue) are plotted for the storms. (The superposed logarithmic average of a

quantity Q is 10^x, where $x = <\log_{10}(Q)>$ is the superposed average of $\log_{10}(Q)$.) The electron flux shows the familiar prestorm decay [*Borovsky and Denton*, 2009a], storm time dropout [*Borovsky and Denton*, 2009b], and then recovery and growth during the storm [*Borovsky and Denton*, 2010a]. The superposed average of the 1 MeV proton flux shows a shift to higher fluxes from before the storm onset to after the storm onset. Note that this increase in the average proton flux commences nearly 1 day prior to the storm onsets. It is possible that this early increase in the superposed average of the 1 MeV proton flux at geosynchronous orbit is caused by increases in the fluxes of solar wind energetic protons associated with corotating interaction regions [cf. *McDonald et al.*, 1975; *Reames et al.,* 1991; *Richardson*, 2004], producing a mild SPE-like effect; this possibility will be investigated further at the end of this subsection.

In Figure 10 (second panel) the superposed logarithmic averages of the number densities of the radiation belt protons (blue) and electrons (red) are plotted for the storms. The electron density shows (1) a decay before the storm, (2) a dropout near the onset of the storm, (3) a recovery of density early in the storm, and then (4) reaching a constant density, four evolutionary stages that are familiar from the studies of the electron radiation belt at geosynchronous orbit with SOPA [*Borovsky and Denton*, 2010b, 2011a]. In Figure 10 (second panel) the superposed average of the density of radiation belt protons (blue) shows a constant density prior to storm onset and a shift to higher density during the storms. In Figure 10 (second panel) (triggered on storm onset as seen by *Kp*) this proton radiation belt density increase looks like a gradual shift to higher density but in individual events it is usually a sudden jump to higher density. This sudden proton radiation belt density increase will be investigated in section 4.2.

In Figure 10 (third panel) the superposed logarithmic averages of the radiation belt temperatures (spectral hardnesses) for protons and electrons are plotted. The electrons (red) show a constant temperature during the density decay before the storm, a drop in temperature when the radiation belt density recovers, and a slow heating during the duration of the storm, all signatures that are familiar from the studies of the electron radiation belt at geosynchronous orbit with SOPA [*Borovsky and Denton*, 2010b, 2011a]. The superposed average of the proton temperature shows an increase commencing before storm onset and a return to average values shortly after storm onset. This slight day-or-two enhancement of the proton radiation belt temperature might be caused by enhanced solar wind energetic proton fluxes associated with the corotating interaction regions (see analysis below).

In Figure 11 the superposed averages of Figure 10 are replotted from 40 days prior to storm onset to 40 days after storm onset where the 27 day repeating nature of the behavior can be seen. The center vertical dashed line marks the storm onsets, and the other two vertical dashed lines are located 27 days before and after the storm onsets. In Figure 11 (fourth panel) the 27 day repeating activation of the *Kp* index is seen and in the red curves of the first to third panels clear 27 day repeating enhancements of the 1 MeV electron flux, the electron radiation belt number density, and the electron radiation belt temperature are seen. The electron dropout signatures that are seen at the storm onsets in Figure 11 (second panel) are too narrow in time to be seen in the 27 day repetition since the repeat periods vary somewhat from storm to storm as coronal hole features on the solar surface evolve with time. In the blue curve of Figure 11 (first panel) the step increase in the 1 MeV proton flux shows a 27 day repeating pattern and in the second panel the enhancement of the proton radiation belt number density after storm onset shows a 27 day repeating pattern. In Figure 11 (third panel), the slight temperature increase of the proton radiation belt near storm onset is too small to show a 27 day repeat.

The contamination of the geosynchronous proton measurements by enhanced proton fluxes in the solar wind associated with corotating interaction regions is investigated in Figure 12. Here for a subset of the 94 high-speed stream-driven storms the superposed logarithmic averages of the proton radiation belt temperature and of the fluxes of energetic protons in the solar wind as measured by the IMP-8 spacecraft are plotted. Only IMP-8 energetic proton measurements that have been screened to eliminate magnetospheric contamination (since IMP-8 spends part of its orbit in the magnetosphere) are used: those screened IMP-8 measurements are available in the OMNI2 data set [*King and Papitashvili*, 2005] prior to 1988. Hence, the subset is 45 of the 94 storms in the years 1976–1987. In Figure 12 (bottom) the superposed averages of the solar wind integral proton fluxes for three energies are plotted. A slight 2 daylong enhancement in the solar wind fluxes is seen commencing slightly before $t = 0$; similarly, a 2 daylong enhancement of the measured proton temperature at geosynchronous orbit is seen in Figure 12 (top). The signatures in Figure 12 (top and bottom) are not identical, but the data coverage of CPA and of IMP-8 going into the superposed averages is not

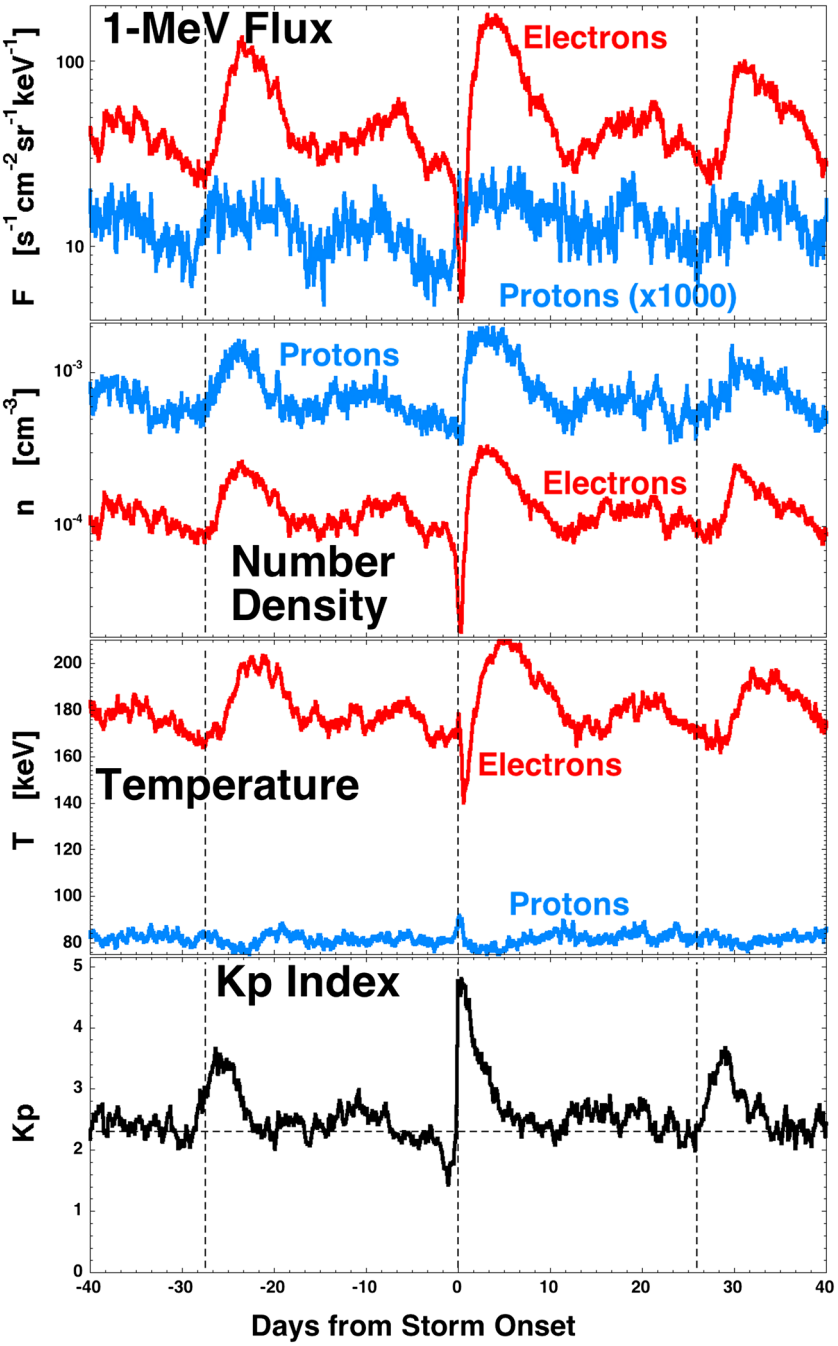

Figure 11. Same plot as Figure 10 but with the time axis expanded to ±40 days from storm onset. The vertical dashed lines are 27 days apart. In Figure 11 (first to third panels) the superposed averages are superposed logarithmic averages.

identical. Figure 12 is strongly suggestive that enhanced solar wind fluxes of energetic protons associated with CIRs could be the origin of the tendency to have enhanced proton radiation belt temperature seen during the CIR portion of high-speed stream-driven storms. This is discussed further in section 5.4.2.

4.2. Radiation Belt Density Dropouts and Density Enhancements

Several of the points discussed in section 4.1 about the proton and electron radiation belts will become clearer in this section when the superposed averaging is triggered on the times of dropouts and recoveries of the radiation belt densities.

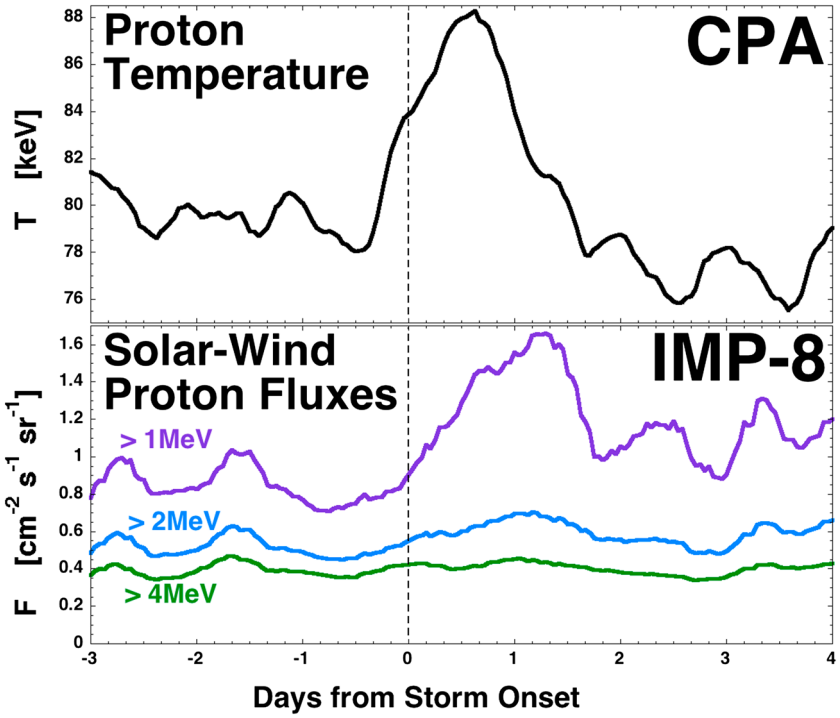

Figure 12. For 45 storms in the years 1976–1987 (see Table 2) that had screened IMP-8 data, (top) the superposed average of the proton radiation belt temperature at geosynchronous orbit and (bottom) the fluxes of energetic protons in the solar wind are plotted. All local times are utilized for the geosynchronous measurements. In both panels the superposed averages are superposed logarithmic averages.

As seen in Figures 10 and 11, the radiation belt electrons during high-speed stream-driven storms show distinct density dropouts [cf. *Freeman*, 1964; *Nagai,* 1988; *Onsager et al.,* 2002; *Green et al.,* 2004; *Borovsky and Denton*, 2009a; *Morley et al.,* 2010] followed by density recoveries [*Borovsky and Denton*, 2010a, 2010b, 2011a; *Denton et al.*, 2010]. Figures 13 and 14 will show that those electron density dropout and recovery features are much more abrupt than they appear in Figure 10.

In Figure 13 the superposed epoch averaging is triggered on the identified onset times of electron density dropouts in the storm collection. Not all storms produce electron dropouts, and the depths and widths of the dropouts can vary [e.g., *Selesnick,* 2006; *Borovsky and Steinberg*, 2006; *Borovsky and Denton*, 2009b; *Morley et al.,* 2010]; additionally, data gaps preclude the identification of dropout onset times for some storms. Forty-eight of the 94 storms that showed strong dropouts identified on the multiple spacecraft available are used for superposed averaging in Figure 13. As can be seen by the red electron radiation belt curve in Figure 13 (fourth panel), the dropouts are abrupt. The 1 MeV electron flux (second panel) drops abruptly with the density dropout, and the electron temperature (third panel of Figure 13) becomes slightly elevated as the density drops. Figure 13 (first panel) plots the superposed average of the *AE* index: as seen the electron density dropout in Figure 13 (fourth panel) tends to occur in the rising levels of geomagnetic activity near the onset of the geomagnetic storm.

Of the two proposed mechanisms for storm time electron dropout ((1) magnetopause shadowing [e.g., *Desorgher et al.,* 2000; *Ukhorskiy et al.,* 2006; *Shprits et al.,* 2006; *Kim et al.,* 2008] and (2) pitch angle scattering into the atmosphere [e.g., *Cornwall et al.,* 1970; *Fraser and Nguyen,* 2001; *Meredith et al.,* 2003; *Jordanova et al.,* 2006; *Thorne et al.,* 2006]), the research community favors magnetopause shadowing caused by the combination of (a) an inward movement of the magnetopause by enhanced solar wind ram pressure and (b) enhanced radial diffusion has been gaining favor [e.g., *Turner et al.,* 2012; *Yu et al.,* 2013; *Ozeke et al.,* 2014]. Note in Figure 13 (third panel) that the robust dropout of the number density of the electron radiation belt (red curve) is not accompanied by a strong dropout of the number density of the proton radiation belt [see also *Green et al.*, 2004]. Similarly in Figure 13 (second panel), there is a clear dropout of the 1 MeV electron flux but not of the 1 MeV proton flux. (On the contrary, an examination of a CME-driven storm by *Turner et al.* [2014]

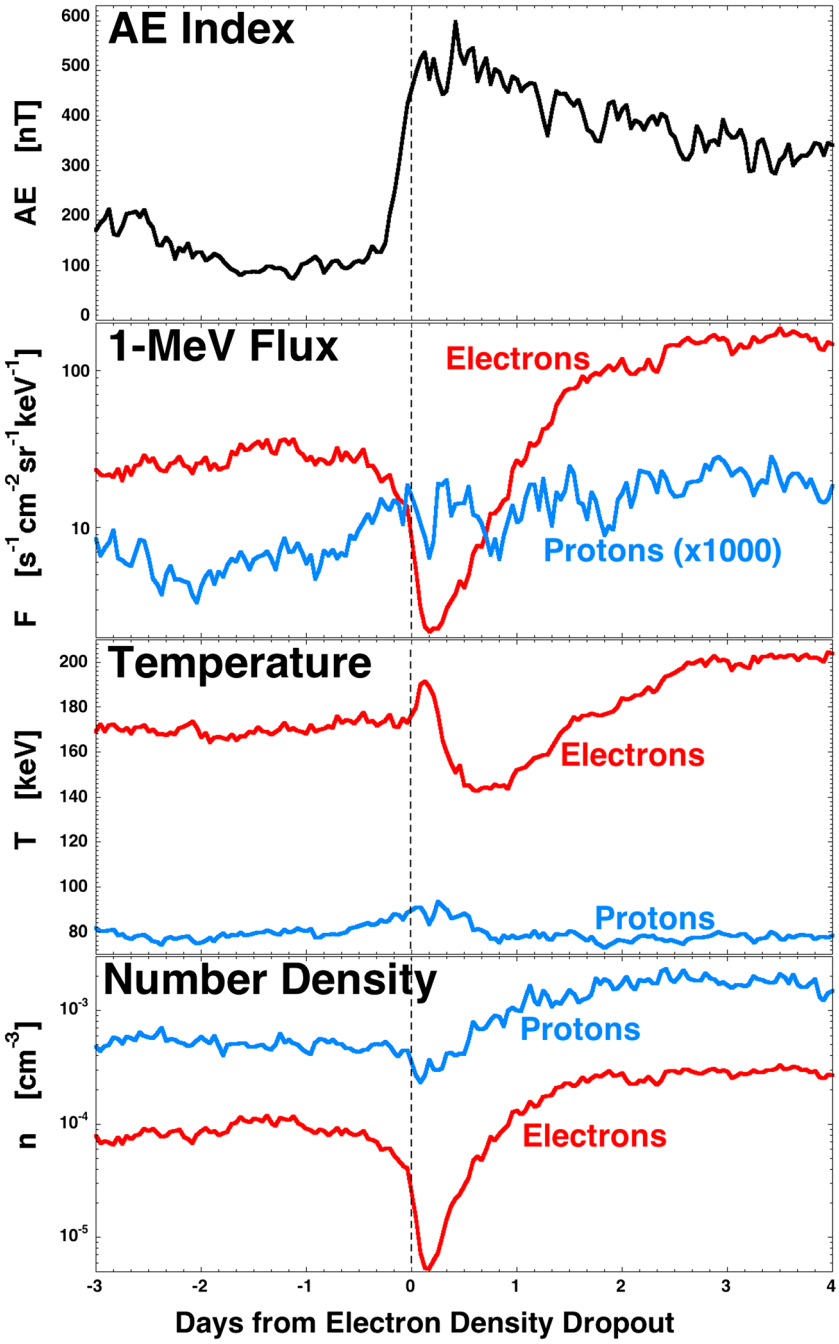

Figure 13. For 48 clear electron radiation belt density dropouts in the 94 storms of Table 2, superposed averages are plotted with the zero epoch being the onset time of the electron density dropout. (first panel) The *AE* index, (second panel) the 1 MeV proton and electron flux, (third panel) the radiation belt temperature, and (fourth panel) the radiation belt number density. In Figure 13 (second to fourth panels) the superposed averages are superposed logarithmic averages.

does find a proton dropout accompanying an electron dropout.) For the high-speed stream-driven storms examined here, the lack of proton dropouts poses a dilemma if the electron dropout is caused by magnetopause shadowing: the azimuthal drift speeds for protons and electrons at 1 MeV are about the same [cf. *Schultz and Lanzerotti*, 1974, Figure 6], and so the geosynchronous orbit 1 MeV electrons and the geosynchronous orbit 1 MeV protons should have very similar radial diffusion coefficients and should simultaneously both be showing losses to the magnetopause. When the 94 individual storms are examined for rapid decreases in the proton radiation belt density, such signatures are rare. The storms do, however,

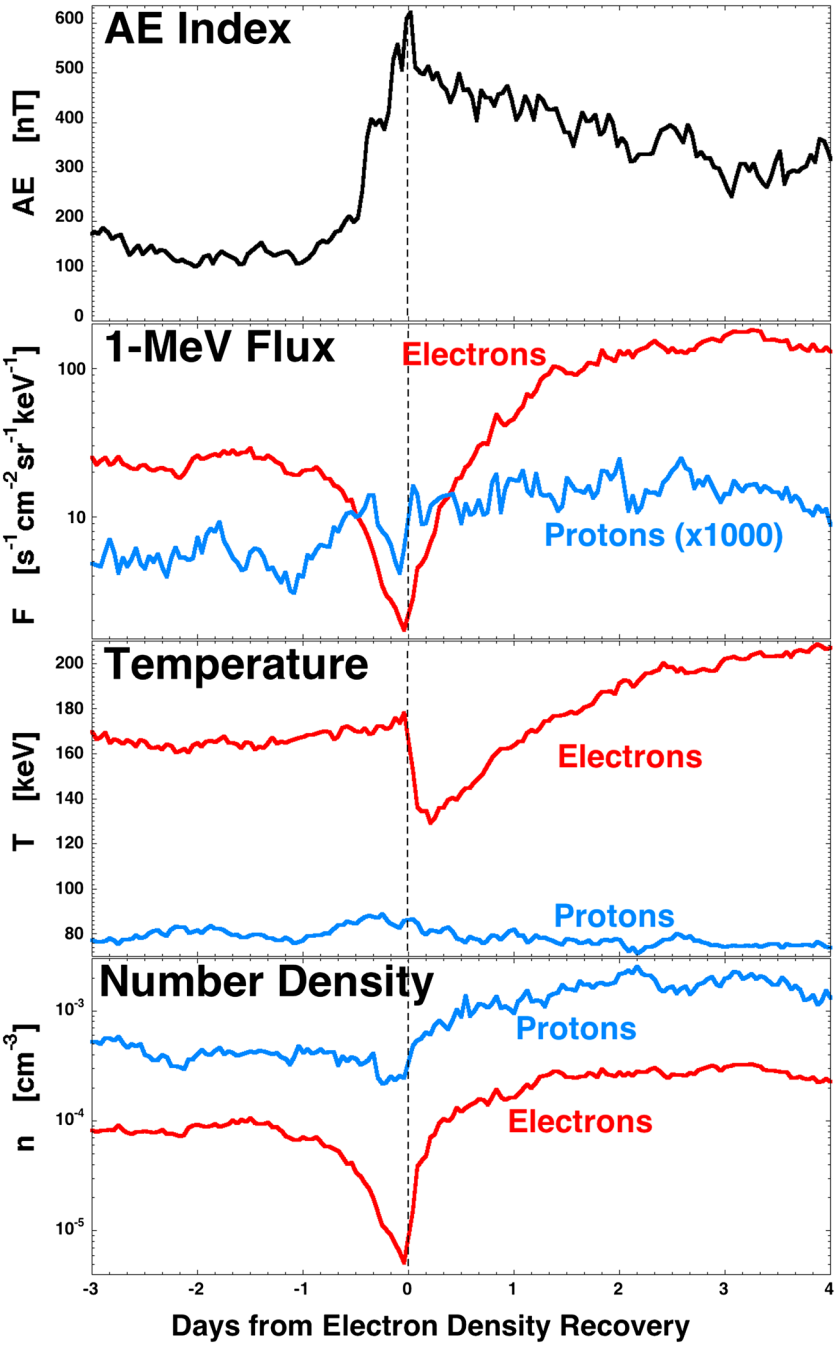

Figure 14. For 47 clear electron radiation belt density recoveries in the 94 storms of Table 2, superposed averages are plotted with the zero epoch being the onset time of the electron density recovery. (first panel) The *AE* index, (second panel) the 1 MeV proton and electron flux, (third panel) the radiation belt temperature, and (fourth panel) the radiation belt number density. In Figure 14 (second to fourth panels) the superposed averages are superposed logarithmic averages.

show prominent signatures of abrupt enhancements of the number density of the proton radiation belt; these enhancements will be investigated later in this section, after the electron enhancements are investigated.

In Figure 14 the superposed epoch averaging is triggered on the time of electron radiation belt density recovery, using 47 of the 94 storms that had prominent identifiable recovery times. The abruptness of the density recovery can be seen in the red curve in Figure 14 (fourth panel), where the electron radiation belt density rapidly increases and then levels out to a constant value during the storm. Note two things about the electrons at the time of the density recovery. First, the superposed average of the temperature of the

electron radiation belt drops (Figure 14, third panel) as the density increases: this indicates that the electrons moving into geosynchronous orbit to form the density recovery are cooler than the electrons that were there before the dropout. Second, the majority of the increase of the 1 MeV electron flux (Figure 14, second panel) occurs much later than the electron density recovery. This large increase of the electron flux is associated with a slow but steady increase in the temperature of the electron radiation belt (Figure 14, third panel) during the several daylong high-speed stream-driven geomagnetic storm [*Borovsky and Denton*, 2010a], about 24 keV per day of temperature change in Figure 14. In Figure 14 (first panel) the superposed average of the *AE* index is plotted triggered on the number density recovery of the electron radiation belt. Note the localized peak in the superposed average of *AE* at the time of the electron density recovery; this peak is suggestive of the occurrence of a substorm at the time of electron radiation belt density recovery. (Note that a peak in the superposed *AE* index is not seen in Figures 9 or 13 where the triggering is on storm onset and on electron dropout.) Examining the available 1 min resolution auroral-electrojet-index data for the 47 electron density recoveries, it is found that 37/45 = 82% of the enhancements are temporally associated with sudden increases in the magnitudes of *AL* and *AE* that are consistent with substorm expansion phases. The sudden increases in the *AL* and *AE* magnitudes that are temporally correlated with the sudden density recoveries of the outer electron radiation belt are typically a few hundreds of nT in size: these strong stretching phase substorms are not extremely large substorms by auroral-electrojet standards. Substorms that occur later in the high-speed stream-driven storms have noticeably larger auroral-electrojet amplitudes.

As seen in Figure 14 (fourth panel), there is an enhancement of the superposed average of the number density of the proton radiation belt associated with the abrupt recovery of the electron radiation belt density. By focusing the superposed epoch averaging on the times of sudden proton density recovery, this proton density enhancement is investigated in Figure 15.

In Figure 15 the superposed epoch averaging is triggered on the time of abrupt density increase of the proton radiation belt during the storms. Twenty-eight of the 94 storms that showed prominent rapid increases in the proton radiation belt density near storm onset were used in Figure 15. In Figure 15 (fourth panel) the superposed average of the number density of the proton radiation belt is plotted in blue; note the sudden increase by about a factor of 3 of the superposed average. In Figure 14 (fourth panel) a similar increase in the superposed average of the number density of the electron radiation belt is seen at the time of the proton density increase. Comparing the fourth panels of Figures 14 and 15, the electron density increase follows a prominent dropout (decrease) (cf. Figure 14), whereas a much weaker proton density decrease precedes the density enhancement of the protons (cf. Figure 15). In Figure 15 (second panel) the superposed averages of the 1 MeV differential fluxes of protons (blue) and electrons (red) at geosynchronous orbit are plotted. Note the sudden increase of the 1 MeV proton flux at the time of the density increases. A similar increase in the 1 MeV flux of electrons is seen, but that increase is dwarfed by the electron flux increase during the first 2 days of the high-speed stream-driven storm (see also Figure 10). In Figure 15 (first panel) the superposed average of the *AE* index is plotted, triggered on the time of the density increase of the proton radiation belt. Note the very distinct localized peak in the average of *AE* at the trigger time: this is suggestive of enhanced probability of the occurrence of a substorm at the time of increase of the proton radiation belt. Indeed, examination of the available 1 min resolution auroral-electrojet-index data for the 28 proton density enhancements finds that 24/25 = 96% of the enhancements are temporally associated with sudden increases in the magnitudes of *AL* and *AE* that are consistent with substorm expansion phases. As was the case for the electron density recoveries discussed above, the sudden increases in the *AL* and *AE* magnitudes that are temporally correlated with the density enhancements of the outer proton radiation belt are typically a few hundreds of nT in size, so these strong stretching phase substorms are not extremely large substorms by auroral-electrojet standards. Substorms that occur later in the high-speed stream-driven storms have noticeably larger auroral-electrojet amplitudes.

In Figures 16–21 four examples of proton density increases and electron density increases will be examined in detail. In these examples the raw proton and electron count rates in the CPA instruments will be scrutinized to see the reactions during the density recoveries. Three conclusions will be yielded by Figures 16–21: (1) the radiation belt density increases are associated with the occurrence of a substorm during the strong stretching phase of the storm, (2) there are clear increases of the electron and proton count rates occurring over a broad range of particle energies, and (3) protons and electrons of up to 1 MeV are injected into geosynchronous orbit at the onset time of this strong stretching phase substorm.

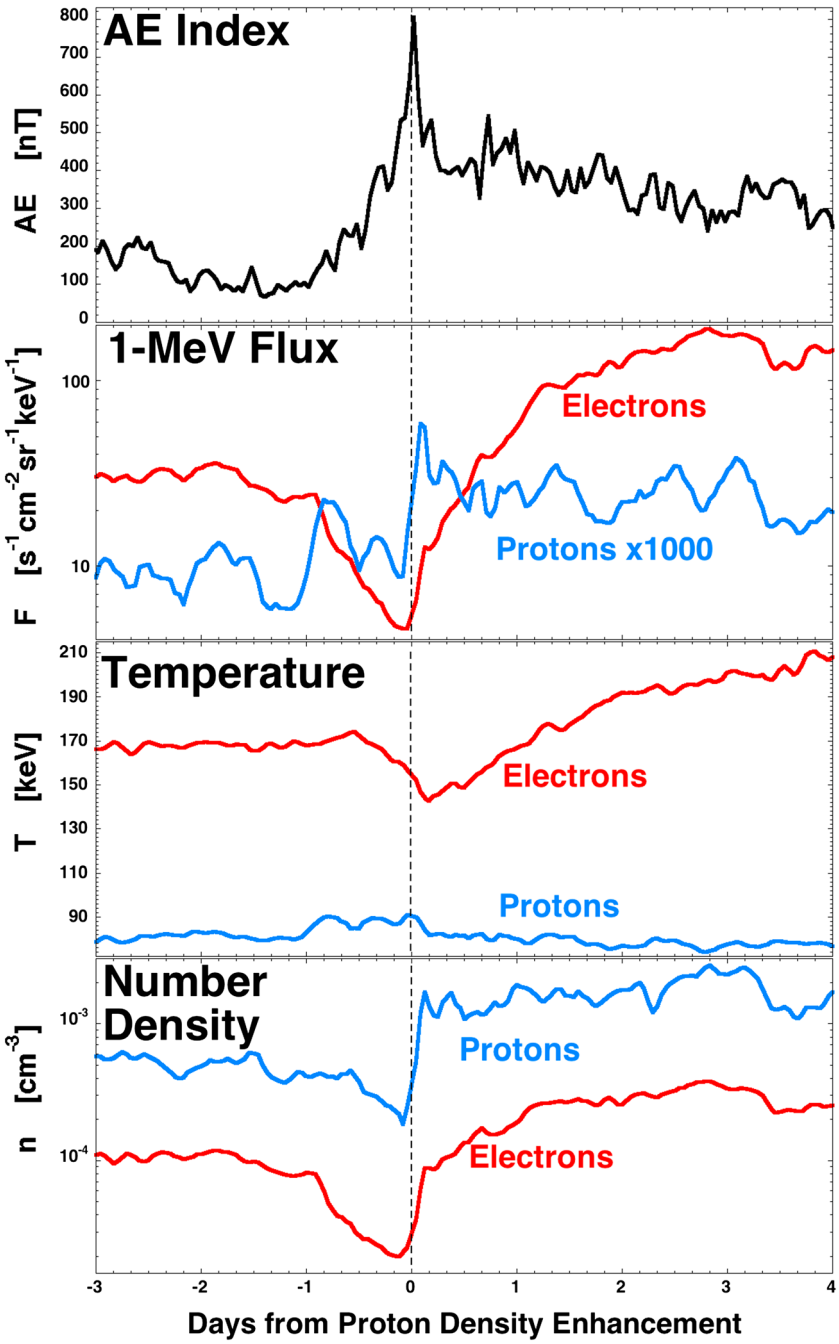

Figure 15. For 28 clear proton radiation belt density enhancements in the 94 storms of Table 2, superposed averages are plotted with the zero epoch being the onset time of the proton density enhancement. (first panel) The *AE* index, (second panel) the 1 MeV proton and electron flux, (third panel) the radiation belt temperature, and (fourth panel) the radiation belt number density. In Figure 15 (second to fourth panels) the superposed averages are superposed logarithmic averages.

This substorm association investigated with two examples of proton radiation belt increases in Figures 16 and 17. A proton radiation belt density enhancement near the onset of a high-speed stream-driven storm on Day 157 (June 6) of 1985 is investigated in Figure 16. In the 30 min resolution CPA data set, the proton radiation belt density increase occurs between 15:15 UT and 15:45 UT on Day 157. In Figures 16a–16c log-log plots of the proton count rates in the CPA detectors onboard three geosynchronous spacecraft versus the mean energies of the proton channels; the lower nine channels measure integral fluxes (that channel and the higher-energy

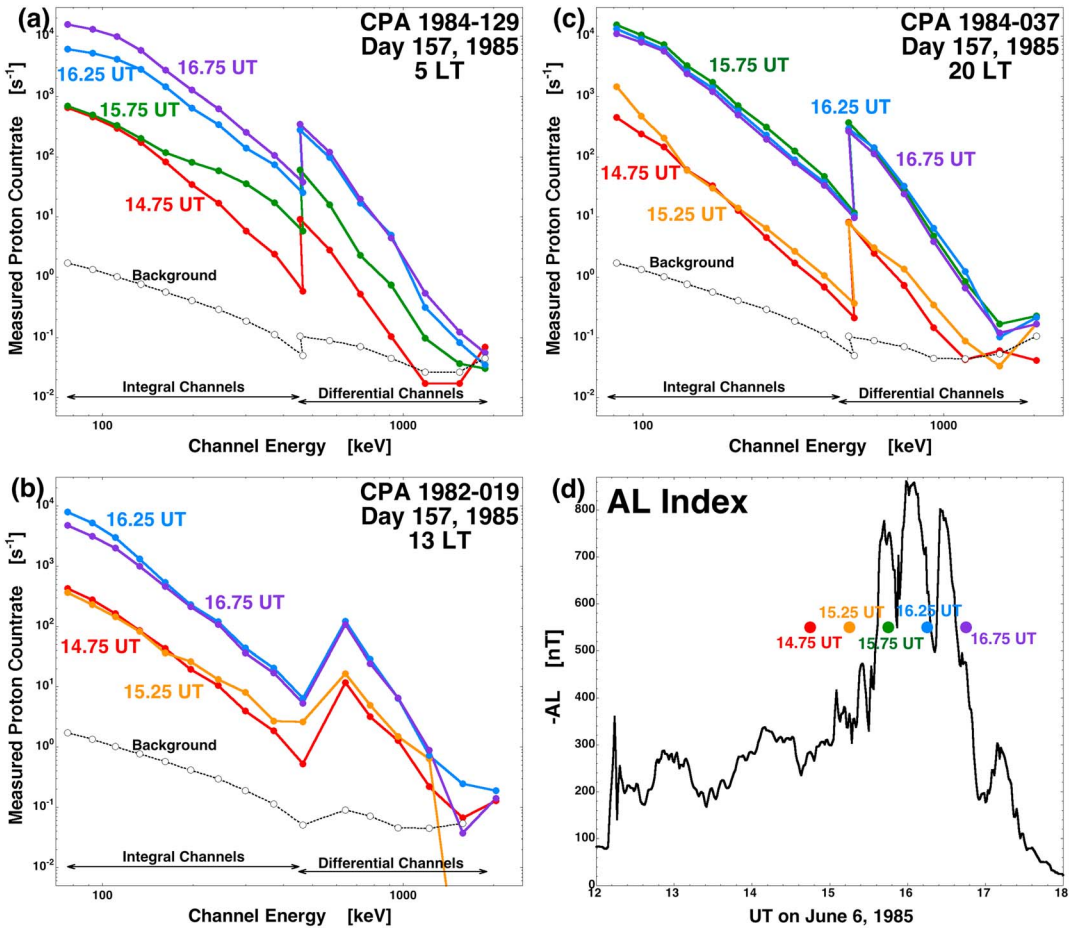

Figure 16. For a proton radiation belt density enhancement on Day 157 (June 6) 1985, the proton count rates in 20 energy channels are plotted from (a–c) three geosynchronous spacecraft before and after the enhancement. Note that the low-energy channels (integral) and the high-energy channels (differential) have different geometric factors, hence the step in the count rate versus energy. (d) $-AL$ is plotted as a function of time with the times of the count rate plots denoted as the colored dots.

channels) and the higher six channels measure differential fluxes. The step in the count rates at ~500 keV is due to the difference in geometric factors between the CPA low-energy detectors and the CPA high-energy detectors: it is not a jump in the differential fluxes in the magnetosphere. The measured count rates are plotted at five different times in five different colors. For spacecraft 1984-037 located at about 20 LT (Figure 16c) an enhancement of the count rates at all energies up to 1 MeV is clear, with that enhancement occurring between 15.25 and 15.75 UT on Day 157: the red and orange curves have lower count rates and the green, blue, and purple curves have higher count rates. The enhancement of the count rates is also seen at dawn (Figure 16a) (on spacecraft 1984-129) and on the dayside (Figure 16b) (on spacecraft 1982-019). In Figure 16d the *AL* index ($-AL$) is plotted as a function of time for 6 h on Day 157. A rapid rise in the magnitude of *AL* commencing at about 15:30 to 15:34 UT is indicative of the onset of a substorm [cf. *Tanskanen et al.,* 2001; *Weygand et al.,* 2008]. The times at which the CPA count rate curves are made are marked as the five colored points in panel Figure 16d. The red and orange curves with the lower count rates were created from measurements taken before the substorm onset, and the green, blue, and purple curves with higher count rates were created from measurements taken after the substorm onset. The green curve in Figure 16a at dawn appears to be making the transition from low count rates to high count rate, whereas it has fully made the transition in (Figure 16c) near the nightside. Energetic ions drift counter to the rotation of Earth, going from the nightside to dusk to noon and then to dawn with the highest energies traveling the fastest. The shape of the green curve in Figure 16c reflects this, with the higher energies having made more of the low-to-high transition than the lower energies. Unfortunately, there were no data on spacecraft 1982-019 to make the 15.75 UT curve at local noon.

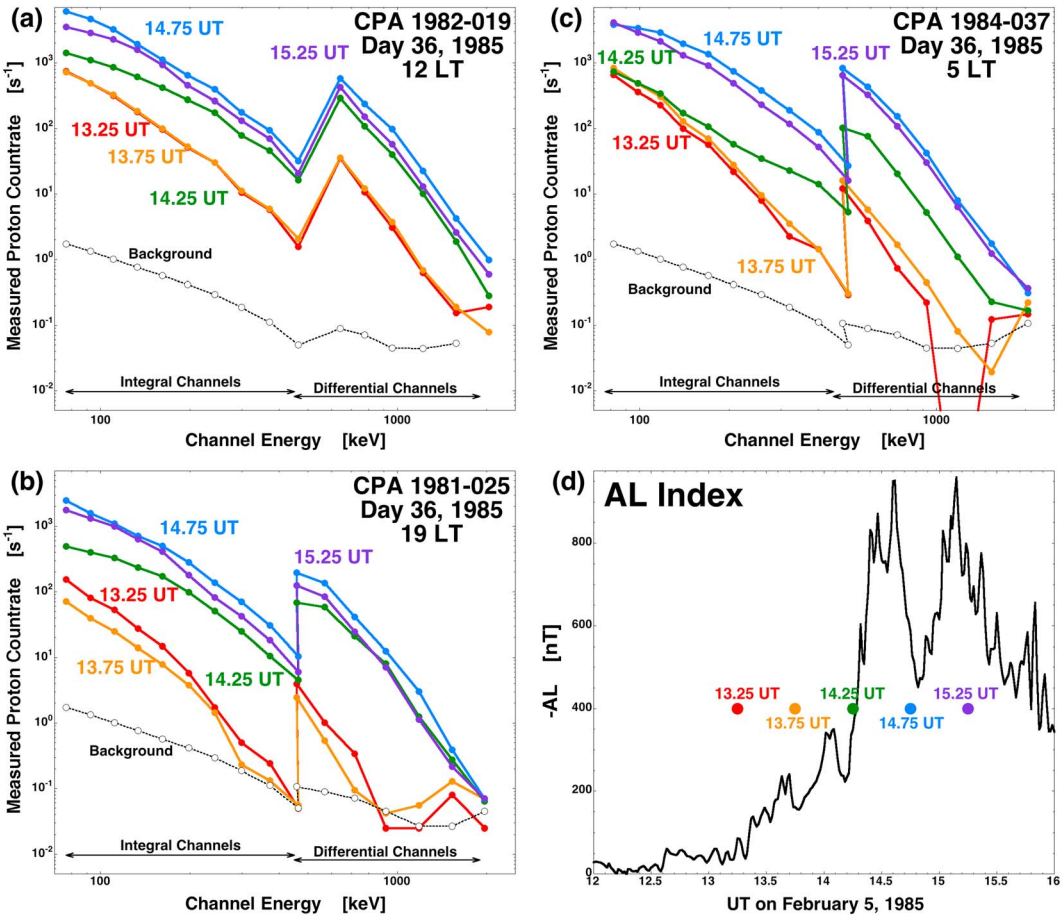

Figure 17. For a proton radiation belt density enhancement on Day 36 (February 5) 1985, the proton count rates in 20 energy channels are plotted from (a–c) three geosynchronous spacecraft before and after the enhancement. Note that the low-energy channels (integral) and the high-energy channels (differential) have different geometric factors. (d) $-AL$ is plotted as a function of time with the times of the count rate plots denoted as the colored dots.

A second proton density enhancement near the onset of a high-speed stream-driven storm on Day 36 (February 5) of 1985 is investigated in Figure 17. The density increase commences at about 13:45 UT on February 5. In Figures 17a–17c proton count rate curves are created at five different times and plotted in five different colors. All three geosynchronous spacecraft (at dusk (Figure 17b), dawn (Figure 17c), and dayside (Figure 17a)) see an enhancement of the proton count rates at all energies up to and beyond 1 MeV somewhere between 13.75 UT and 14.75 UT on Day 36. In Figure 17d $-AL$ is plotted as a function of time for 4 h on Day 36, with the times at which the five count rate curves were produced marked as the five colored points. A large rise in the magnitude of *AL* that commences at about 14:13 UT is indicative of the onset of a substorm. As can be seen in Figure 17d, the low count rate curves (13.25 UT and 13.75 UT) were produced prior to the substorm onset and the high count rate curves (14.75 UT and 15.25 UT) were produced after the substorm onset. The 14.25 UT curve (which is produced from data taken in the time interval 14.0–14.5 UT) shows a transition in Figures 17a–17c that varies with local time; in Figure 17d it is seen that the substorm onset is within that half hour from 14.0 UT to 14.5 UT. The green curve appears least evolved (from low count rates to high count rates) at dawn (Figure 17c) (spacecraft 1984-037) compared with dusk (Figure 17b) and local noon (Figure 17a): the shapes of the green transition time curves indicate the higher energies being more fully transitioned than the lower energies, commensurate with the nightside to dusk to noon to dawn sense of travel for ions and with higher-energy ions traveling faster.

In Figures 18 and 19 the count rates of the energetic electrons as measured by CPA instruments in geosynchronous orbit are examined for the Day-157 and Day-36 proton radiation belt density enhancements of Figures 16 and 17. In Figures 18a–18c for the Day-157 proton enhancement a temporal transition to higher

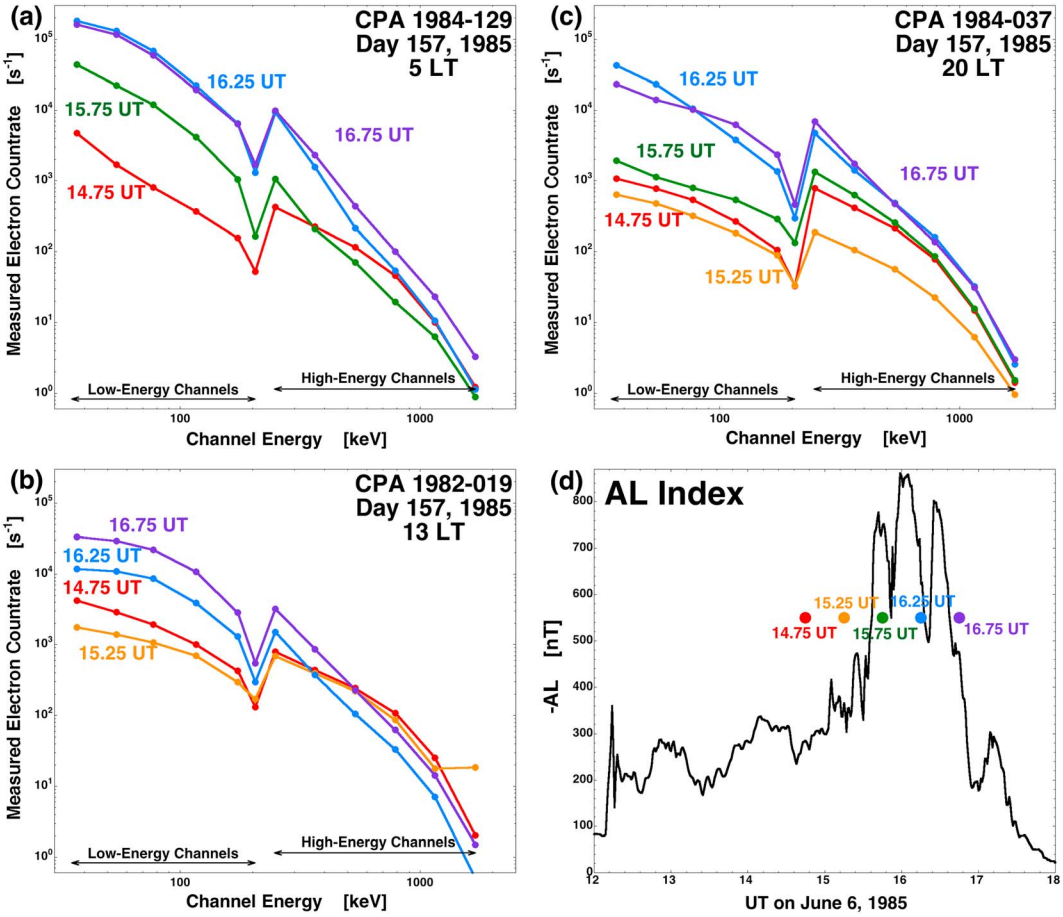

Figure 18. For the proton radiation belt density enhancement on Day 157 (June 6) 1985 (see Figure 16), the electron count rates in 12 energy channels are plotted from (a–c) three geosynchronous spacecraft before and after the enhancement. Note that the low-energy channels and the high-energy channels have different geometric factors. (d) $-AL$ is plotted as a function of time with the times of the count rate plots denoted as the colored dots.

electron count rates is seen at all three spacecraft (dawn, dayside, and dusk), and the enhancement of the electron count rates extends up to 1 MeV. (The step in the count rates at ~200 keV is due to the difference in geometric factors between the CPA low-energy detectors and the CPA high-energy detectors.) Detailed comparisons between the proton count rate curves of Figure 16 and the electron count rate curves of Figure 18 for each of the spacecraft show that the enhancement in the electron count rates comes slightly later in time than the enhancement of the ion count rates. The electron count rates for the Day-36 proton radiation belt density enhancement in Figure 19 also show the distinct enhancement at all energies up to 1 MeV. Comparison between the proton count rates (Figure 17) and the electron count rates (Figure 18) again shows the result that the proton enhancement occurs prior to the electron enhancement (note the green curve in all panels).

Two sudden recoveries of the number density of the electron radiation belt (cf. Figure 14) are examined in Figures 20 and 21. For an electron density recovery event on Day 185 (July 4) of 1985, electron count rates are plotted at six different times in Figures 20a–20c. A transition in electron count rates at energies up to and beyond 1 MeV is seen on the nightside (Figure 20a) (1984-129), prenoon (Figure 20b) (1982-019), and at dusk (Figure 20c) (1984-037). The *AL* index plot in Figure 20d indicates a substorm onset at about 12:03–12:06 on Day 185. The 12.25 UT count rate curves (green) are made from the half hour of data that spans the onset (12.0–12.5 UT). Note in Figures 20a–20c that the green curve has not made the transition from low count rates to high count rates, except at the highest energies on 1984-129 near local midnight (Figure 20a). The electron count rate transition for the electron density recovery on Day 185 seems to occur somewhat after substorm onset begins. The case is different for an electron density recovery on Day 224

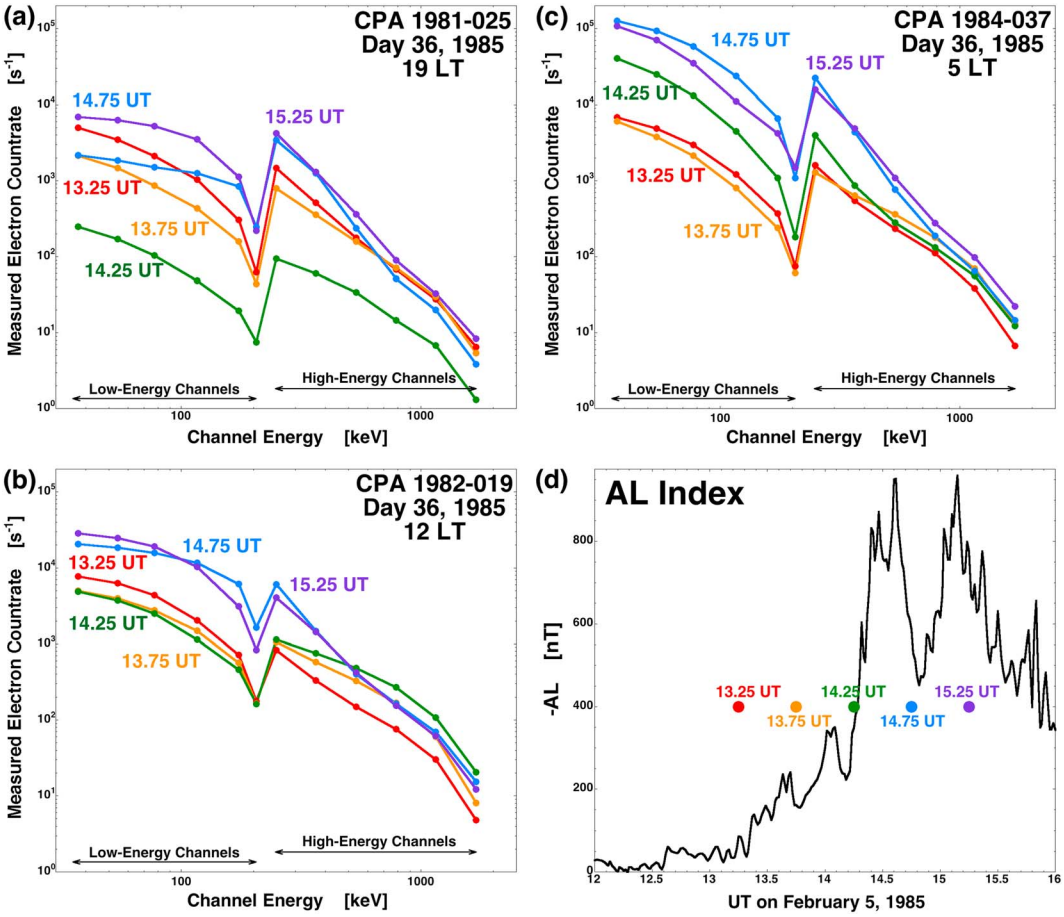

Figure 19. For the proton radiation belt density enhancement on Day 36 (February 5) 1985 (see Figure 17), the electron count rates in 12 energy channels are plotted from (a–c) three geosynchronous spacecraft before and after the enhancement. Note that the low-energy channels and the high-energy channels have different geometric factors. (d) $-AL$ is plotted as a function of time with the times of the count rate plots denoted as the colored dots.

(August 12) of 1985; in Figures 21a–21c the clear transition from lower count rates to higher count rates occurs within the half hour that contains the onset (at about 23:04) of the substorm as seen in the *AL* index in Figure 21d.

Note in Figures 20 and 21 that the energy spectra of the high-energy electrons are noticeably softer after the count rate enhancements than before the count rate enhancements. This is in agreement with the decrease in the temperature (decrease in hardness) of the electron radiation belt as the density recovers (cf. Figure 14, second panel).

The sudden delivery of a new electron radiation belt population and a new proton radiation belt population to geosynchronous orbit during storm time substorms will be discussed further in section 5.2

5. Discussion

In this section a number of relevant topics are discussed.

5.1. Where in the Timing of the CIRs and High-Speed Streams Do Radiation Belt Density Dropouts and Density Enhancements Occur?

To discern this timing, the properties of pertinent solar wind parameters will be examined with respect to the dropouts and recoveries. The pertinent solar wind measurements that are available in the CPA era are the solar wind speed v_{sw} (for determining the timing of the slow-to-fast wind transition across the CIR), the solar wind flow longitude φ_{sw} (for determining the timing of the east-west flow deflection in the CIR), the solar

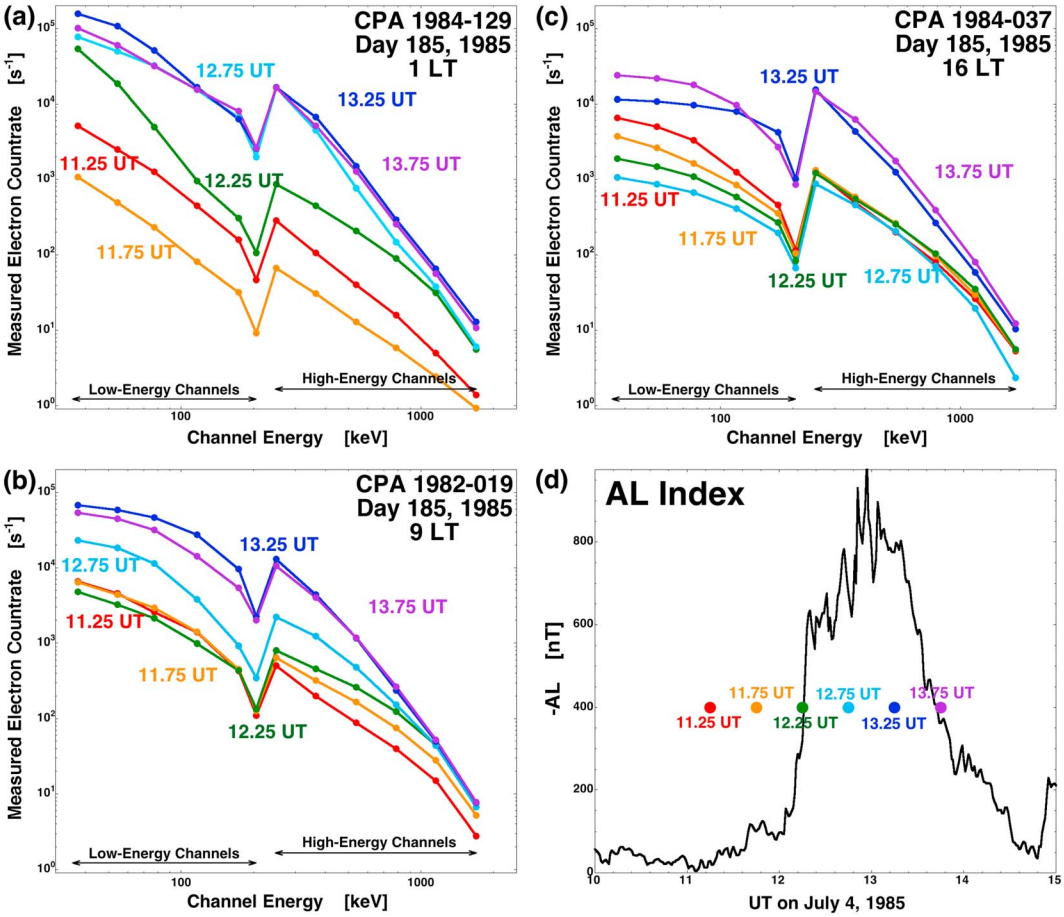

Figure 20. For an electron radiation belt density recovery on Day 185 (July 4) 1985, the electron count rates in 12 energy channels are plotted from (a–c) three geosynchronous spacecraft before and after the enhancement. Note that the low-energy channels and the high-energy channels have different geometric factors. (d) $-AL$ is plotted as a function of time with the times of the count rate plots denoted as the colored dots.

wind magnetic field strength B_{mag} (for determining the extent of the CIR compression and the location of the peak compression [*Borovsky and Denton*, 2010c, 2013]), the solar wind density n_{sw} (for determining the importance of ram pressure), and the proton specific entropy $S_p = T_{sw}/n_{sw}^{2/3}$ (for determining the transition from low-entropy streamer belt plasma to high-entropy coronal hole origin plasma [cf. *Intrilligator and Siscoe*, 1994; *Borovsky and Denton*, 2010c]). Note that T_{sw} is the proton temperature of the solar wind. Solar wind measurements from the OMNI2 database [*King and Papitashvili*, 2005] will be used.

In Figure 22 the superposed averages of those solar wind measurements are plotted with the zero epoch being the onset time of the electron radiation belt density dropout (same zero epoch as in Figure 13). In Figure 22 (first panel) the superposed average of the solar wind speed v_{sw} is plotted; it is seen that the electron dropouts ($t = 0$) are occurring on average during the early portion of the rising solar wind velocity, in the early portion of the CIR. This is corroborated by Figure 22 (second panel) where it is seen that the electron dropouts are occurring prior to the reversal in the east-west (dawnward-duskward) flow of the solar wind. That reversal of the flow through zero is approximately the location of the CIR stream interface separating streamer belt plasma from coronal hole plasma [*Siscoe et al.,* 1969; *Gosling et al.,* 1978; *Borovsky and Denton*, 2010c]. Hence, the electron radiation belt dropouts are occurring, while compressed streamer belt plasma or compressed sector-reversal-region plasma is passing the Earth prior to the passage of the stream interface. This is also confirmed by the red and green curves in Figure 22 (fourth panel); the red S_p curve shows the dropouts occurring in low-entropy (streamer belt or sector-reversal-region) solar wind [cf. *Xu and Borovsky,* 2015], and the green B_{mag} curve shows that the dropouts occur before the peak of the compression of the CIR. The blue n_{sw} curve in Figure 22 (fourth panel) indicates that the temporal occurrence of the electron radiation belt density

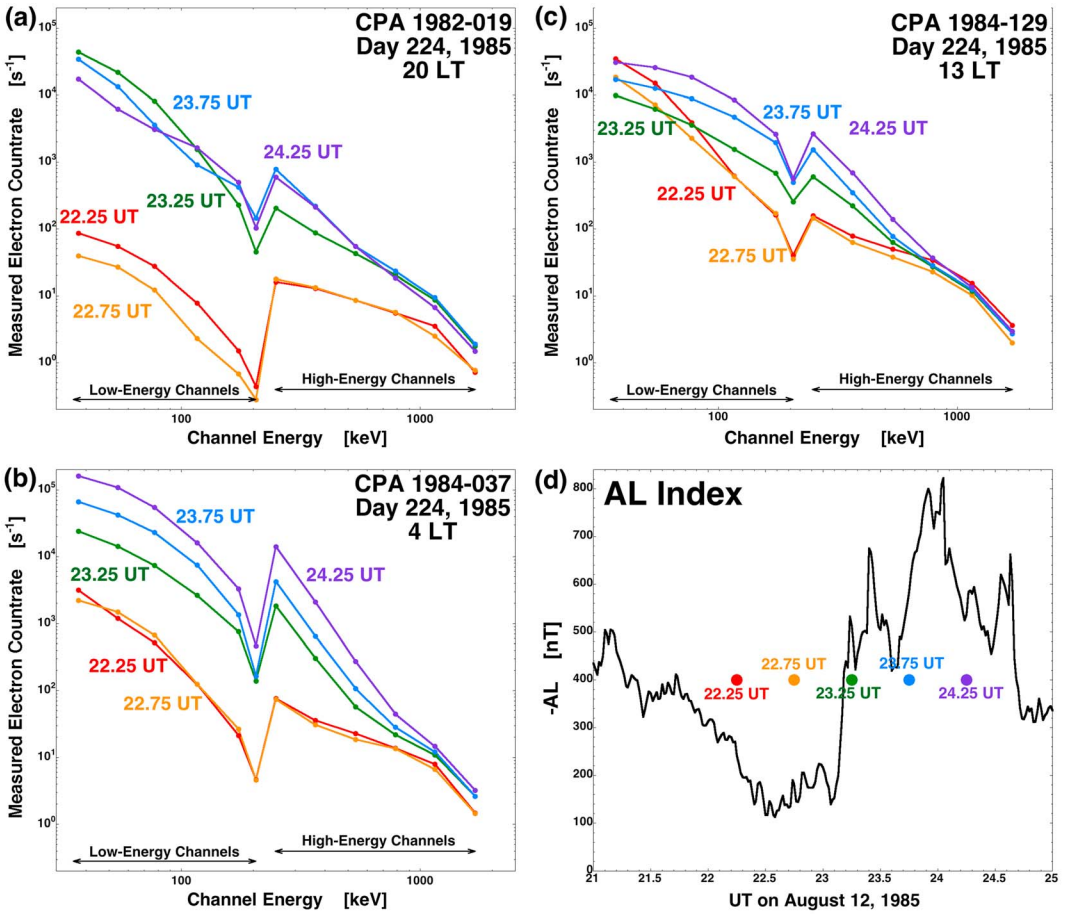

Figure 21. For an electron radiation belt density recovery on Day 224 (August 12) 1985, the electron count rates in 12 energy channels are plotted from (a–c) three geosynchronous spacecraft before and after the enhancement. Note that the low-energy channels and the high-energy channels have different geometric factors. (d) $-AL$ is plotted as a function of time with the times of the count rate plots denoted as the colored dots.

dropout is associated with a peak of the solar wind number density, which also corresponds to a peak in the solar wind ram pressure. Earlier studies [e.g., *Onsager et al.*, 2007; *Borovsky and Denton*, 2010b] also found that dropouts of the electron radiation belt were associated with ram pressure temporal peaks in the solar wind. Figure 22 (third panel) plots the superposed average of the *Newell et al.* [2007] universal driver function for the magnetosphere $v^{4/3}B_t^{2/3}\sin^{8/3}(\theta/2)$, where $B_t = (B_y^2 + B_z^2)^{1/2}$ in the upstream solar wind and where θ is the IMF clock angle. The driver function makes a transition from low values prior to the CIR to higher values during and after the CIR compression; this transition is because of the Russell-McPherron effect and the probable occurrence of a magnetic sector reversal within or just prior to the CIR [*Borovsky and Steinberg*, 2006; *McPherron et al.*, 2009]. As seen in Figure 22 (third panel), values of the superposed average of the driver function are ~2000 before the CIR transitioning to ~8000 after the CIR. Dropout of the relativistic electron flux is synonymous with dropout of the density of the electron radiation belt; prior studies have reported that the electron flux dropouts occur in the compressed slow wind prior to the passage of the stream interface [cf. *Borovsky and Denton*, 2009b, Figure 2; *Morley et al.*, 2010, Conclusion 1; and *Kilpua et al.*, 2015, Figure 3.

In Figure 23 the superposed averages of the solar wind measurements are plotted with the zero epoch being the onset of the electron radiation belt density recovery (same zero epoch as Figure 14). Figure 23 (first panel) shows that the electron density recoveries occur on average later in the rise of solar wind speed from slow to fast. The second panel shows that the electron radiation belt density recoveries tend to occur after the dawnward-duskward reversal through zero of the solar wind flow direction, i.e., after the CIR stream interface passes, in what is compressed coronal hole origin solar wind plasma. This is corroborated by the red S_p curve in Figure 23 (fourth panel) showing that the electron number density recoveries occur in high-entropy

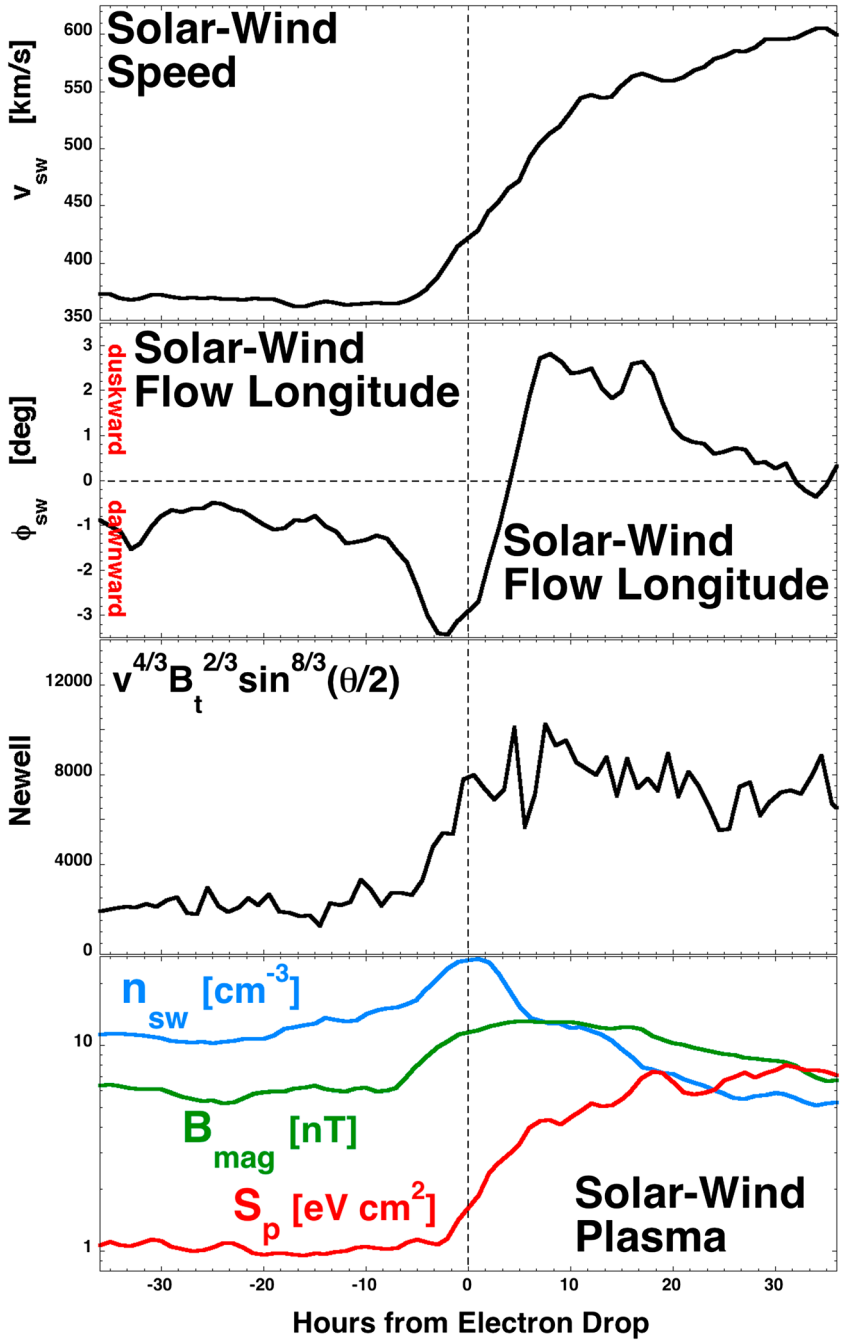

Figure 22. For 48 clear geosynchronous orbit electron radiation belt density dropouts in the 94 storms of Table 2, superposed averages are plotted with the zero epoch being the onset time of the electron density dropout. (first panel) The solar wind speed at Earth, (second panel) the solar wind east-west flow vector longitude at Earth, (third panel) the Newell universal driver function, and (fourth panel) the number density, proton specific entropy, and magnetic field strength of the solar wind at Earth. In Figure 22 (third panel) the superposed average of S_p is a superposed logarithmic average.

coronal hole plasma [*Xu and Borovsky*, 2015]. The green curve in Figure 23 (fourth panel) shows that the electron recoveries tend to occur after the peak compression (maximum of B_{mag}) of the CIR, which occurs near the stream interface. The blue n_{sw} curve in Figure 23 (fourth panel) indicates that the electron radiation belt density recovery is occurring when the solar wind density has subsided to lower levels. Hence, the electron number density recoveries are occurring within the CIR, in compressed coronal hole plasma, just after the passage of the stream interface. Note that there have been earlier studies of the location of the recovery

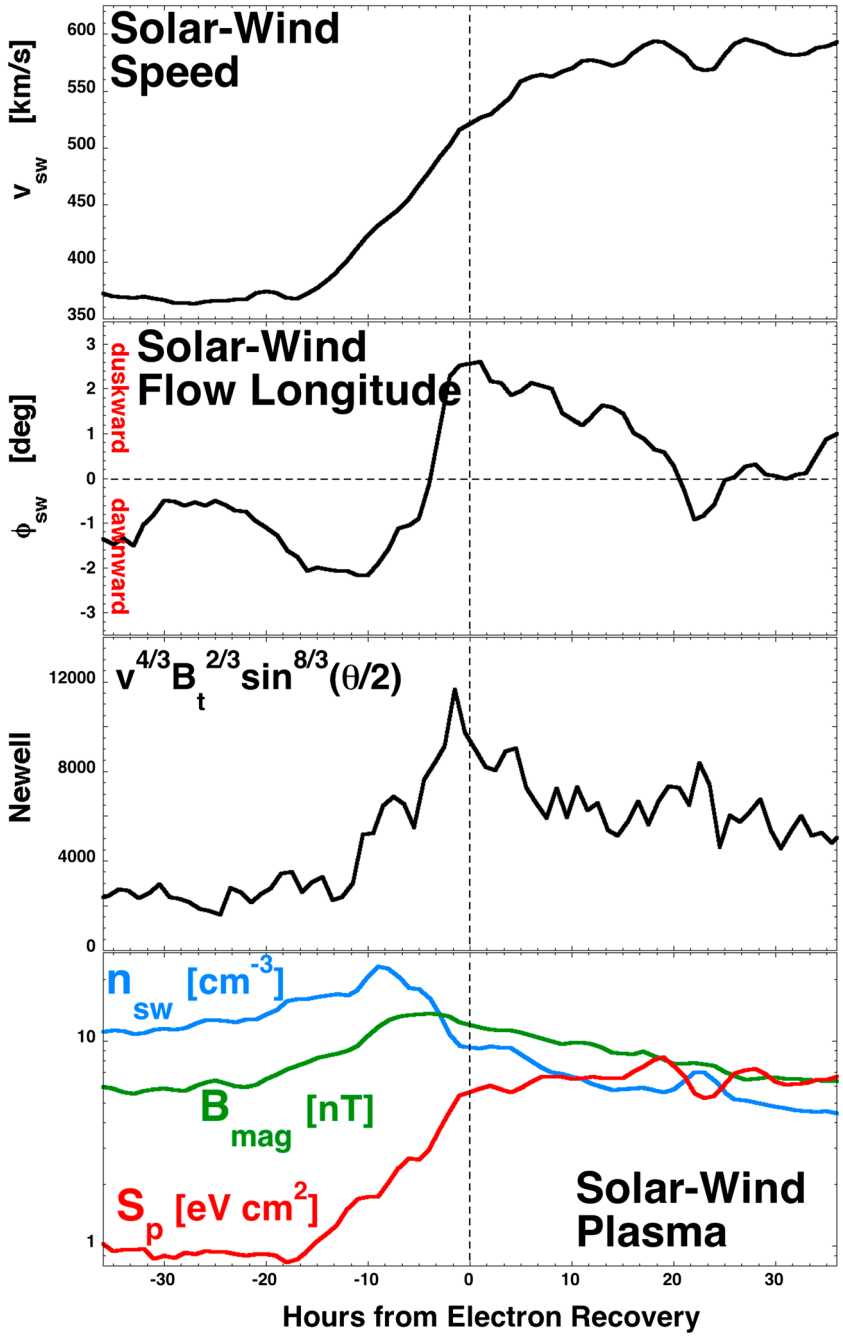

Figure 23. For 47 clear geosynchronous orbit electron radiation belt density recoveries in the 94 storms of Table 2, superposed averages are plotted with the zero epoch being the onset time of the electron density recovery. (first panel) The solar wind speed at Earth, (second panel) the solar wind east-west flow vector longitude at Earth, (third panel) the Newell universal driver function, and (fourth panel) the number density, proton specific entropy, and magnetic field strength of the solar wind at Earth. In Figure 23 (third panel) the superposed average of S_p is a superposed logarithmic average.

of the relativistic electron flux in high-speed stream-driven storms; however, the electron flux recovery is not the same as the electron density recovery [cf. *Borovsky and Denton*, 2010b]: the flux recovery comes after the density recovery. Those earlier studies [*Borovsky and Denton*, 2009b; *Kilpua et al.*, 2015] found that the relativistic electron flux begins to recover in the CIR sometime after the passage of the stream interface. Figure 23 (third panel) plots the superposed average of the universal driver function $v^{4/3}B_t^{2/3}\sin^{8/3}(\theta/2)$: note the sharp peak in the superposed average about 1.5 h prior to the onset of the radiation belt electron density recovery

(with a 1 h time binning in the superposed averaging). Owing to the rapid variations in the direction of the solar wind magnetic field, the driver function varies rapidly with time in the individual time series going into the superposed average. This peak in the superposed average is because times of stronger driving are being lined up together in the averaging process. One suspects that picking zero epochs that are the electron density recovery times is related to picking zero epochs that are substorm occurrence times and that the peak in the superposed average in Figure 23 (third panel) is the relation of strong intervals of driving to the subsequent occurrence of substorms.

In Figure 24 the superposed averages of the solar wind measurements are plotted with the zero epoch being the onset time of the proton radiation belt density enhancement (same zero epoch as Figure 15). The timing results for the proton density enhancement (Figure 24) are similar to the timing results for the electron density recovery (Figure 23): Figure 24 (first panel) indicates that the proton density enhancement occurs within the interval of rising solar wind speed, the second panel indicates the proton density enhancement tends to occur after the stream interface, and the fourth panel indicates that the proton density enhancement tends to occur after the solar wind density begins to subside (blue curve) and in compressed high-entropy (coronal hole origin) plasma (red curve). Figure 24 (third panel) plots the superposed average of the universal driver function $v^{4/3}B_t^{2/3}\sin^{8/3}(\theta/2)$. Similar to the case in Figure 23, Figure 24 (third panel) shows a sharp peak in the superposed average about 0.5 h prior to the onset of the radiation belt electron density recovery (with a 1 h time binning in the superposed averaging). The interpretation of this peak is the same interpretation as that of Figure 23, only stronger. The peak is caused by the zero epoch being temporally associated with to the occurrence of a substorm, and the peak is the short-term strong solar wind driving that produces the substorm [e.g., *Morley and Freeman*, 2007; *Boakes et al.,* 2011]; choosing the zero epoch to be proton density recoveries is related to choosing the zero epoch to be a substorm occurrence (but not just any substorm).

To summarize, the density dropout of the electron radiation belt tends to occur when the solar wind number density (and solar wind ram pressure) is maximum in the early portion of the CIR prior to the passage of the stream interface, when compressed streamer belt origin or sector-reversal-region plasma is passing the Earth. The density recoveries of the electron radiation belt and the density enhancements of the proton radiation belt both tend to occur later in the CIR after the passage of the stream interface when compressed coronal hole origin plasma is passing the Earth. The electron radiation belt density dropouts tend to occur while the solar wind velocity vector is perturbed dawnward, and the electron radiation belt density recovery and proton radiation belt density enhancements tend to occur while the solar wind velocity vector is perturbed duskward.

5.2. Proton Radiation Belt Sources and Electron Radiation Belt Sources During Storm Time Substorms

Early-storm injections of radiation belt electrons were seen in the SOPA geosynchronous data set when a cooler population of radiation belt electrons arrives at geosynchronous orbit to produce a sudden global enhancement of the electron radiation belt number density [*Borovsky and Denton*, 2010b, 2011a]; following that injection the electron radiation belt at geosynchronous orbit is slowly heated at constant number density during the days of the high-speed stream-driven storm to produce a gradual increase in the flux of energetic electrons in the days following storm onset [*Borovsky and Denton*, 2010a, 2011a].

Using the CPA proton and electron measurements, in section 4.2 this injection phenomena was seen for both the electron radiation belt and the proton radiation belt at geosynchronous orbit. In section 4.2 the injections were specifically seen to occur in conjunction with the occurrence of substorms in the early phases of high-speed stream-driven storms (cf. Figures 16–22). These storm time substorms produced enhancements in the protons at geosynchronous orbit to energies beyond 1 MeV and produced enhancements of the electrons at geosynchronous orbit at energies to 1 MeV (cf. Figures 16–22).

The early phases of high-speed stream-driven storms are characterized by a strong stretching phase associated with the presence of the superdense plasma sheet early in the storm [*Borovsky and Denton*, 2010b]. The strong stretching phase, which lasts about 1 day, gets its name from a nightside magnetic field morphology at geosynchronous orbit that is tail like rather than dipolar; this strong stretching phase of the storm is associated with the presence of a diamagnetic superdense plasma sheet early in the storm [*Borovsky et al.,* 1997], with the origin of the superdense plasma sheet being the magnetospheric capture of enhanced solar wind densities of the plasma compression in the corotating interaction region leading the high-speed stream [*Denton and Borovsky*, 2009]. In the SOPA studies of the electron radiation belt, it was established that the

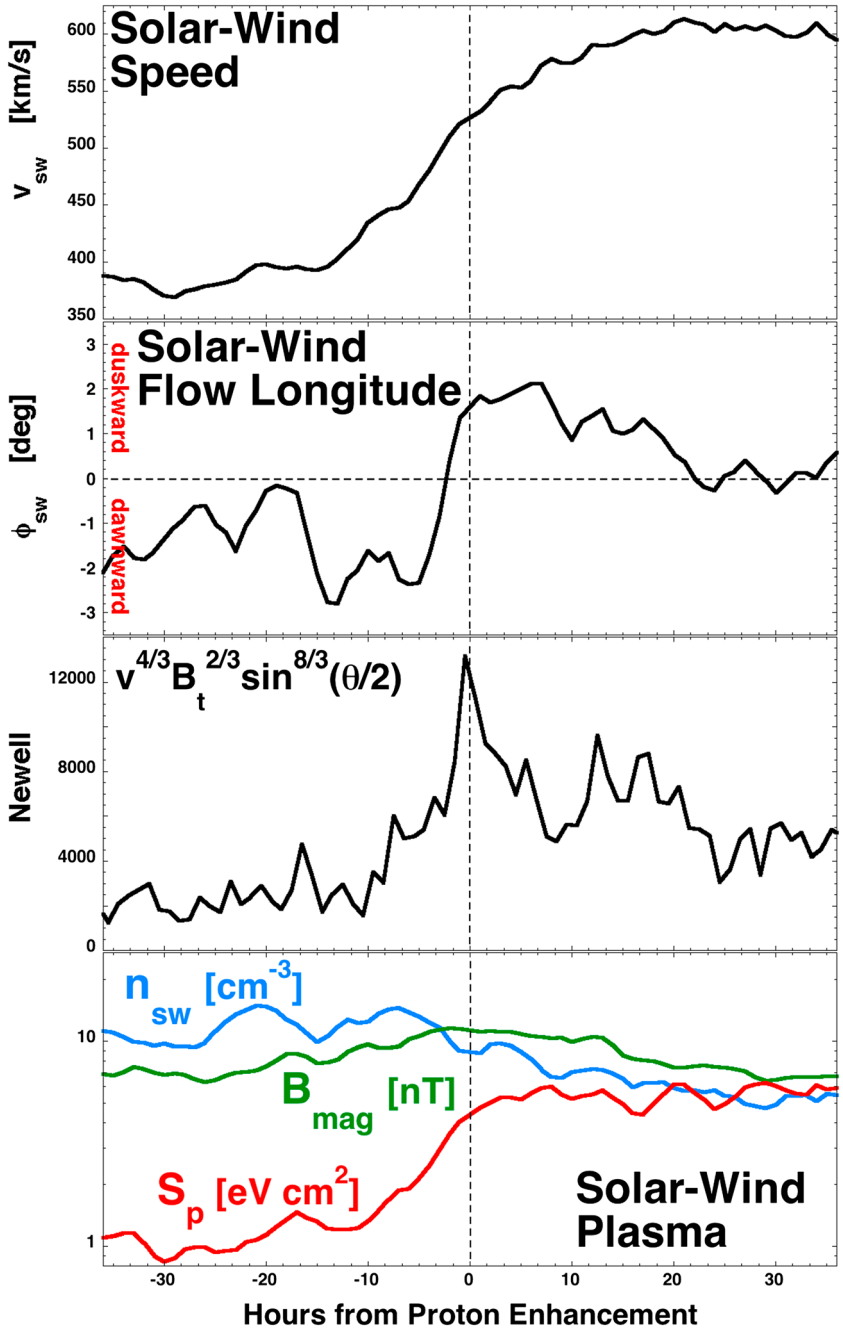

Figure 24. For 28 clear geosynchronous orbit proton radiation belt density enhancements in the 94 storms of Table 2, superposed averages are plotted with the zero epoch being the onset time of the proton density enhancement. (first panel) The solar wind speed at Earth, (second panel) the solar wind east-west flow vector longitude at Earth, (third panel) the Newell universal driver function, and (fourth panel) the number density, proton specific entropy, and magnetic field strength of the solar wind at Earth. In Figure 24 (third panel) the superposed average of S_p is a superposed logarithmic average.

sudden number density enhancement of the electron radiation belt definitely occurs during the strong stretching phase of the storm [cf. *Borovsky and Denton*, 2010b, Figure 21]. The origin of the sudden density enhancement of the electron radiation belt is the direct production of the recovery electron radiation belt population by a substorm; the origin of the sudden density enhancement of the proton radiation belt is also the direct production of the enhanced proton radiation belt population by a substorm.

Increases of proton fluxes with energies up to 1 MeV at geosynchronous orbit in association with the occurrence of a substorm have been reported by *Belian et al.* [1978] using CPA measurements, and increases of electron fluxes with energies up to 1 MeV at geosynchronous orbit in association with the occurrence of a substorm have been reported by *Ingraham et al.* [2001] using CPA measurements. *Birn et al.* [2012] point out the difficulty in understanding how substorm reconnection in the magnetotail could produce such 1 MeV particles: this difficulty exists to the present day (J. Birn, private communication, 2016). It has been suggested (E. Antonova, private communication, 2011) that a substorm injection into a localized minimum in the nightside magnetic field strength can produce an injected electron population of extra-high energies [see also *Antonova et al.,* 2011; *Antonova and Stepanova*, 2015]. Hence, a substorm that occurs during the strong stretching phase of a high-speed stream-driven storm may directly produce the recovery population for the outer electron radiation belt. In the present report, the production of radiation belt electrons and protons up to and beyond 1 MeV has been seen in association with substorms that occur during the strong stretching phase of storms.

As noted in section 4.2, although these strong stretching phase substorms deliver protons and electrons of energies to 1 MeV and above to geosynchronous orbit, the substorms are not extremely large as measured by their sudden increase in the magnitude of the *AL* index or the *AE* index (cf. Figures 14–22). Perhaps, substorms that occur during the strong stretching phase of a storm are not efficient at producing auroral currents near the auroral-electrojet-index magnetometer stations; this could be caused by an equatorward expansion of the auroral oval during the strong stretching phase, placing the auroral-electrojet activations southward from the Northern Hemisphere *AE* stations (J. Birn, private communication 2016).

5.3. The Absence of Proton Radiation Belt Dropouts

Global (at all local time) density dropouts of the electron radiation belt at geosynchronous orbit are common during high-speed stream-driven storms (cf. Figures 10 and 13), with the electron dropouts lasting ~0.5 day. In the superposed averages plotted in Figure 13, which are triggered on the times of density dropouts of the electron radiation belt, significant global dropout of the number density or the 1 MeV flux of the proton radiation belt is not seen. As stated in section 4.2, inspection of the individual storms does not, in general, show global (at all local times) dropouts of the protons. (Brief single-spacecraft dropouts are seen near local midnight during the presubstorm stretching of the nightside magnetic field but no indications of global loss of radiation belt protons.) Note again that *Turner et al.* [2014] reported a proton dropout (lasting least several hours) accompanying an electron dropout during a CME-driven storm.

For the high-speed stream-driven storms, the absence of proton radiation belt dropouts at geosynchronous orbit when there are electron radiation belt dropouts at geosynchronous orbit has implications for the picture of electron radiation belt loss to the magnetopause caused by an Earthward displacement of the dayside magnetopause accompanied by enhanced radial diffusion [e.g., *Shprits et al.,* 2006; *Yu et al.,* 2013; *Ozeke et al.,* 2014]. Since the azimuthal drift speeds and drift periods of 1 MeV protons and 1 MeV electrons at geosynchronous orbit are very similar [cf. *Schultz and Lanzerotti*, 1974, Figure 6], it is anticipated that the radial diffusion coefficients D_{LL} for the electron and proton radiation belts should have similar values for energetic protons and energetic electrons [cf. *Falthammar*, 1973, section 9.8 and *Lanzerotti et al*., 1978, Figure 5]. Hence, radial diffusion loss to the magnetopause should have similar timescales for protons and electrons; if you see loss of electrons, it is expected to be accompanied by loss of protons.

It has been suggested by a reviewer that proton radiation belt dropouts might be occurring but that substorm injections of protons are filling in the radiation belt dropouts in the 30 min resolution measurements used in the present study. That is a possibility that the authors cannot disprove using the 30 min measurements.

The behavior of the radiation belt protons during electron radiation belt dropouts will be the subject of a future study. CPA proton and electron data are available at 1 min resolution. It is also advantageous to study such dropout events in a modern era where additional magnetospheric measurements at geosynchronous orbit are available (including the magnetic field morphology and the presence of the diamagnetic superdense plasma sheet) and where better solar wind measurements are available (including the electron strahl, ion composition, the Alfvenicity, and energetic protons).

5.4. The Role of the Solar Wind in the Evolution of the Electron and Proton Radiation Belts

Since the solar wind controls the magnetosphere-ionosphere system, it is imperative to highlight the connection between solar interplanetary structures and the response of the Earth's radiation belts. In this subsection

the solar wind causes for the evolutions of the outer electron radiation belt and the outer proton radiation belt during high-speed stream-driven storms will be identified.

5.4.1. The Electron Radiation Belt and the Solar Wind

The evolution of the electron radiation belt during high-speed stream-driven storms is characterized by a sequence of four phases, each of which can be associated with a reaction of the magnetosphere to changes in the solar wind. These four phases are discussed in the following four paragraphs.

First, there is a prestorm decay of the density (and fluxes) of the outer electron radiation belt. (This can be seen slightly in Figure 10). The decay may start a day or a few days before the onset of the storm. This prestorm density decay is associated with the refilling of the outer plasmasphere during a geomagnetic calm before the storm [*Borovsky and Denton,* 2009a] (cf. Figures 9 and 10, fourth panels). The calm before the storm is caused by geomagnetically unfavorable IMF clock angles prior to the passage of a heliospheric sector reversal ahead of the CIR stream interface [*Borovsky and Steinberg*, 2006]. A sector reversal only occurs for helmet streamer CIRs [*Crooker et al.,* 2012]; hence, the calm before the storm tends to occur for helmet streamer CIR driven storms. Pseudostreamer CIRs drive geomagnetic storms that tend not to have a calm before the storm and hence tend not to have a prestorm decay of the outer electron radiation belt [*Borovsky and Denton,* 2013].

Second, there is a dropout in the density and flux of the outer electron radiation belt early in the storm. The electron radiation belt dropout is temporally associated with high-density (high ram pressure) solar wind passing the Earth [*Onsager et al.*, 2007], as was seen in Figure 22 (fourth panel). The high ram pressure pushes the dayside magnetopause inward, enabling magnetopause shadowing (with radial diffusion) to strongly deplete the outer electron radiation belt. The high-density solar wind is due to lumps of high-density plasma prior to the passage of the CIR stream interface, plus CIR compression of the solar wind plasma. The high-density lumps are associated with sector-reversal-region plasma [*Xu and Borovsky*, 2015], which is present for helmet streamer CIRs but not for pseudostreamer CIRs. The lumps at 1 AU may be the "blobs" of plasma imaged near the Sun lifting off the tops of streamer stalks [*Wang et al.,* 2000; *Suess et al.,* 2009]. Since helmet streamer CIRs have dense sector-reversal-region plasma and pseudostreamers do not have sector-reversal-region plasma, helmet streamer CIR storms tend to have electron radiation belt density dropouts that are stronger than those of pseudostreamer CIR storms [*Borovsky and Denton,* 2013]. Note that the absence of a strong proton radiation belt dropout when there is a strong electron radiation belt dropout (e.g., Figures 10 and 13) may require closer consideration of this dropout explanation utilizing magnetopause shadowing with radial diffusion (cf. section 5.3). One alternative was proposed by *Borovsky and Denton* [2009b] wherein the anomalously high-density solar wind produces a superdense plasma sheet in the magnetosphere that drives EMIC waves (or magnetosonic waves [*Thomsen et al.,* 2011]) in the plasmaspheric drainage plume to produce anomalous electron radiation belt scattering into the atmosphere to produce the dropout.

Third, there is a sudden density recovery of the outer electron radiation belt early in the storm (cf. Figures 10 and 14). This density recovery is temporally associated with the occurrence of a substorm during the strong stretching phase of the storm (cf. sections 4.2 and 5.1) and with a temporally localized interval of strong solar wind driving (cf. section 5.1). The magnetosphere's strong stretching phase is caused by the diamagnetism of the superdense plasma sheet, and the superdense plasma sheet is caused by the high-density solar wind (sector-reversal-region plasma plus compression) leaking into the magnetosphere to create higher than normal plasma sheet densities. There is a time lag of a few hours from solar wind density to geosynchronous orbit plasma sheet density [*Denton and Borovsky*, 2009]; hence, there is a time lag of a several hours between the solar wind density and the strong stretching phase [cf. *Borovsky and Denton*, 2010b, Figure 28]. The substorm and the electron density recovery occur after the passage of the CIR stream interface, while the Earth is bathed in coronal hole origin plasma. The substorm during the strong stretching phase of the storm is undoubtedly associated with the time interval of strong solar wind driving, which is associated with an interval of very effective IMF clock angle (see section 5.4.3).

Fourth, there is a steady heating (hardening of the energy spectra) of the outer electron radiation belt during the several daylong high-speed stream that follows the CIR (cf. Figure 10), provided that the IMF clock angles during the high-speed stream are Russell-McPherron favorable for geomagnetic activity [cf. *McPherron et al.,* 2009]. During the heating phase the relativistic electron fluxes increase, maximize, and then decrease, with the time to maximum being longer for higher energies. The electron radiation belt heating rate is correlated with several parameters [*Borovsky and Denton*, 2010a; *Balikhin et al.,* 2011; *Borovsky and Denton*, 2014,

Figure 7] such as the solar wind speed, the solar wind specific entropy, the levels of fluctuation in the solar wind, the inverse of the solar wind density, the level of magnetospheric convection, and the amplitudes of ULF fluctuations in the magnetosphere. In analyzing the solar wind control of this electron radiation belt heating, discerning cause from correlation has been difficult.

5.4.2. The Proton Radiation Belt and the Solar Wind

Solar proton events (SPEs) are clearly seen at all local times by the CPA ion detectors in geosynchronous orbit; SPEs drive the geosynchronous orbit proton temperature to anomalously high levels. This represents a solar wind energetic ion population getting into the outer magnetosphere at geosynchronous orbit. The higher-energy protons of this population decay out of geosynchronous orbit on the timescale of a fraction of a day after the solar wind proton intensities subside.

During the CIR portion of high-speed stream-driven storms, the temperature of the proton radiation belt at geosynchronous orbit is increased slightly. This temperature increase at geosynchronous orbit appears to be related to enhanced populations of MeV protons in the solar wind associated with corotating interaction regions [cf. *Mewaldt et al.,* 1979; *Reames et al.,* 1991; *Richardson*, 2004]. Presumably, these energetic solar wind protons leak into the magnetosphere to geosynchronous orbit. These CIR-associated MeV protons in the solar wind are accelerated by CIR shock waves in the outer heliosphere [*Palmer and Gosling,* 1978; *Fisk and Lee,* 1980], with the energized protons coming back toward the Sun along the Parker spiral magnetic field lines within the CIR and bathing the Earth while the Earth is in the CIR. (A 1 MeV proton has a velocity that is about 25 times the solar wind flow speed, so it can easily travel sunward and reach the Earth while the Earth is still in the CIR.)

The evolution of the outer proton radiation belt during a high-speed stream-driven storm is characterized by a sudden density enhancement early in the storm; this density enhancement represents a long-lasting shift in the radiation belt density and a long-lasting increase of the energetic proton fluxes at geosynchronous orbit. This sudden proton radiation belt density enhancement is temporally associated with a temporally localized interval of strong solar wind driving along with the occurrence of a substorm during the strong stretching phase of the storm, with the strong stretching phase caused by prior enhanced solar wind density (sector-reversal-region plasma plus compression) producing a superdense plasma sheet in the magnetosphere. The substorm and the proton radiation belt density enhancement occur after the passage of the CIR stream interface while the Earth is bathed in coronal hole origin plasma.

5.4.3. The Critical Storm Time Substorms

The present study has associated the occurrence of a substorm during the strong stretching phase of high-speed stream-driven storms with the density recovery events that are critical for the evolution of the electron and proton radiation belts. These particular substorms were shown in section 4.2 to be associated with rapid delivery of MeV electrons and MeV protons to geosynchronous orbit.

The radiation belt-producing substorm occurs after the passage of the CIR stream interface while the Earth is bathed in coronal hole origin plasma (cf. section 5.1). Coronal hole origin plasma is characterized by large-amplitude Alfvenic fluctuations of the solar wind magnetic field direction and of the solar wind flow vector [*Tsurutani et al.,* 1994; *Crooker and Gosling*, 1999] that take the form of thin current sheets (discontinuities) [*Borovsky*, 2010b]. When a current sheet passes the Earth, the magnetic field orientation of the solar wind at Earth jumps to a new direction [cf. *Bruno et al.*, 2001, Figure 5]; that direction may be favorable for geomagnetic activity or it may be unfavorable for geomagnetic activity. In the advecting coronal hole plasma, the current sheets are temporally separated by 10 min or so [cf. *Borovsky*, 2008 and *Borovsky*, 2012, Table 1], so a typical time interval of IMF orientation has a duration of 10 min or so. It remains to be investigated how the occurrence of these critical early-storm substorms is related to the mesoscale magnetic field structure of the solar wind plasma passing the Earth.

6. Summary of Findings

Below are the findings of this study. In this summary the abbreviations OPRB (outer proton radiation belt) and OERB (outer electron radiation belt) will be used.

6.1. Basic Properties of the Outer Proton Radiation Belt at Geosynchronous Orbit

1. A new reanalysis of the 8-satellite 2-solar cycle (1976–1995) CPA data set of energetic particle measurements at geosynchronous orbit was utilized for a statistical survey and for event analysis. Relativistic Maxwellian fits

to the measured count rates yielded number densities n and temperatures (spectral hardness) T for the OPRB and OERB.

2. Solar proton events (SPEs) have a strong effect on the CPA measurements of the OPRB at geosynchronous orbit. The CPA proton measurements during an SPE are characterized by anomalously high temperatures ($T > 150$ keV). The CPA proton data set was cleaned of SPEs using two SPE catalogs and using IMP-8 measurements of energetic protons in the solar wind.
3. The number density of the OPRB at geosynchronous orbit (~1.7×10^{-3} cm^{-3}) is on average about 10 times greater than the number density of the OERB at geosynchronous orbit (1.7×10^{-3} cm^{-3}).
4. The energy spectrum of the OPRB at geosynchronous orbit (~85 keV) is softer than the energy spectrum of the OERB at geosynchronous orbit (~176 keV).
5. The 1 MeV proton flux at geosynchronous orbit (~0.058 cm^{-2}s^{-1}sr^{-1}MeV^{-1}) is about 1000 times less than the 1 MeV electron flux at geosynchronous orbit (~78 cm^{-2}s^{-1}sr^{-1}MeV^{-1}).
6. The energy density of the OPRB at geosynchronous orbit (~116 eV cm^{-3}) is typically greater than the energy density of the OERB at geosynchronous orbit (~33 eV cm^{-3}).

6.2. Local Time and Solar Cycle Properties

7. The number densities of both the OPRB and OERB are higher on the dayside of geosynchronous orbit than on the nightside. The number densities of both populations peak in the postnoon of local time.
8. The temperatures (spectral hardness) of both the OPRB and OERB are higher on the dayside of geosynchronous orbit than on the nightside. For the OERB the dayside temperature is 10% higher; for the OPRB the dayside increase is a smaller fraction.
9. The 1 MeV fluxes of protons and of electrons are higher on the dayside of geosynchronous orbit than on the nightside. For the protons the dayside fluxes are about a factor of 5 higher, and for the electrons the dayside fluxes are about a factor of 2 higher.
10. The number densities of both the OPRB and OERB at geosynchronous orbit are lowest during solar maxima and highest during solar minima.
11. The temperature (spectral hardness) of the OERB at geosynchronous orbit is highest during the declining phases of the solar cycle and lowest at solar maxima. The solar cycle temperature dependence of the OPRB at geosynchronous orbit is slight.
12. The 1 MeV fluxes of protons and electrons at geosynchronous orbit are highest during the declining phase and solar minima.

6.3. Behavior During High-Speed Stream-Driven Storms

13. A collection of 62 high-speed stream-driven (CIR driven) geomagnetic storms in the years 1976–1992 has been created and utilized for the study of the evolution of the OPRB and OERB. To this new collection, 32 previous collected storms from 1993 to 1995 were added.
14. The familiar four stages of evolution of the OERB at geosynchronous orbit seen with modern data sets are seen during the 1976–1995 high-speed stream-driven storms: (1) a prestorm decay of the number density, (2) a density dropout early in the storm, (3) a rapid density recovery at cooler temperature, and (4) a slow steady heating at constant density. The 1 MeV electron flux decays with the density decay, drops with the density dropout, increases slightly with the density recovery, and increases greatly during the slow heating phase.
15. The evolution of the OPRB at geosynchronous orbit during high-speed stream-driven storms is characterized by a sudden step-like rise (enhancement) in the number density and a step-like increase in the 1 MeV proton flux during the early portions of the storm.
16. The OPRB at geosynchronous orbit does not dropout when the OERB drops out; similarly, the 1 MeV proton flux does not dropout when the 1 MeV electron flux drops out. Since the radial diffusion coefficients for 1 MeV protons and electrons should be approximately equal, this lack of proton dropout may have implications for the picture of electron dropout caused by magnetopause shadowing with enhanced radial diffusion.
17. The temperature of the OPRB increases mildly during the passage of the CIR, with the onset of the temperature increase beginning about a day before the onset of the geomagnetic storm. This geosynchronous orbit temperature increase is temporally associated with enhanced MeV protons in the solar wind produced within CIRs. Presumably, these energetic protons bathing the Earth diffuse into the magnetosphere and are measured by the CPA instruments.

18. Examination of the solar wind finds that the storm time OERB density dropout occurs in the compressed slow wind (streamer belt origin or sector-reversal-region plasma) prior to the passage of the CIR stream interface when the solar wind velocity vector is dawnward from radial.
19. Examination of the solar wind finds that the storm time sudden OERB density recovery (enhancement) occurs in the compressed fast wind (coronal hole plasma) after the passage of the CIR stream interface when the solar wind velocity vector is duskward from radial. The sudden OERB density recovery is temporally associated with a brief interval of strong driving of the magnetosphere by the solar wind.
20. Examination of the solar wind finds that the storm time sudden OPRB density enhancement occurs in the compressed fast wind (coronal hole plasma) after the passage of the CIR stream interface when the solar wind velocity vector is duskward from radial. The sudden OPRB density recovery is temporally associated with a brief interval of strong driving of the magnetosphere by the solar wind.

6.4. Importance of the Substorm During the Strong Stretching Phase of the Storm

21. The sudden enhancement in the OPRB number density and 1 MeV proton flux during a storm is associated with the occurrence of a substorm during the strong stretching early phase of the storm. Examination of individual proton density enhancements finds that the count rates of protons at all energies to 1 MeV and slightly higher are enhanced at all local times by the substorm.
22. The sudden enhancement in the OERB number density (density recovery) and 1 MeV electron flux during a storm is also associated with the occurrence of a substorm during the strong stretching early phase of the storm. This is implied in superposed epoch studies and confirmed by examining examples. Examination of individual electron density enhancements finds that the count rates of electrons at all energies to about 1 MeV are enhanced at all local times by the substorm. The spectral hardness (temperature) of the OERB is softer (cooler) after the substorm injection of the electrons to 1 MeV.

Acknowledgments
The authors wish to thank Elizaveta Antonova, Joachim Birn, and Reiner Friedel for useful conversations. This work was supported at the Space Science Institute by the NASA Heliophysics LWS TRT program via grants NNX14AN90G and NNX16AB75G, by the NSF Solar-Terrestrial Program via grant AGS-1261659, and by the NASA Heliophysics Guest Investigator Program via grant NNX14AC15G and at the University of Michigan by the NASA Geospace SR&T program via grant NNX12AD29G. CPA data are available on request from Tom Cayton at th23cayton@gmail.com.

References

Antonova, E. E., and M. V. Stepanova (2015), The problem of the acceleration of electrons of the outer radiation belt and magnetospheric substorms, *Earth Planets Space*, *67*, 148, doi:10.1186/s40623-015-0319-7.

Antonova, E. E., I. M. Myagkova, M. V. Stapanov, M. O. Riazantseva, I. L. Ovchinnikov, B. B. Mar'in, and M. V. Karavaev (2011), Local particle traps in the high latitude magnetosphere and the acceleration of relativistic electrons, *J. Atmos. Sol. Terr. Phys.*, *73*, 1465, doi:10.1016/j.jastp.2010.11.020.

Baker, D. N., R. D. Belian, P. R. Higbie, and E. W. Hones (1979), High-energy magnetospheric protons and their dependence on geomagnetic and interplanetary conditions, *J. Geophys. Res.*, *84*, 7138–7154, doi:10.1029/JA084iA12p07138.

Baker, D. N., W. Aiello, J. R. Asbridge, R. D. Belian, P. R. Higbie, R. W. Klebesadel, J. G. Laros, and E. R. Tech (1985), Los Alamos energetic particle sensors at geostationary orbit, *AIAA-85-0283*, p. 1.

Balikhin, M. A., R. J. Boynton, S. N. Walker, J. E. Borovsky, S. A. Billings, and H. L. Wei (2011), Using the NARMAX approach to model the evolution of energetic electrons fluxes at geostationary orbit, *Geophys. Res. Lett.*, *38*, L18105, doi:10.1029/2011GL048980.

Belian, R. D., D. N. Baker, P. R. Higbie, and E. W. Hones (1978), High-resolution energetic particle measurements at 6.6 R_E, 2. High-energy proton drift echoes, *J. Geophys. Res.*, *83*, 4857–4862, doi:10.1029/JA083iA10p04857.

Belian, R. D., G. R. Gisler, T. Cayton, and R. Christensen (1992), High-Z energetic particles at geosynchronous orbit during the great solar proton event series of October 1989, *J. Geophys. Res.*, *97*, 16,897–16,906, doi:10.1029/92JA01139.

Belian, R. D., T. E. Cayton, R. A. Christiansen, J. C. Ingraham, M. M. Meier, G. D. Reeves, and A. J. Lazarus (1996), Relativistic electrons in the outer-zone: An 11 year cycle; their relation to the solar wind, in *AIP Proceedings 383 Workshop on the Earth's Trapped Particle Environment*, edited by G. D. Reeves, 13 pp., Am. Inst. of Phys., Woodbury, New York.

Beutier, T., D. Boscher, and M. France (1995), SALAMBO: A three-dimensional simulation of the proton radiation belt, *J. Geophys. Res.*, *100*, 17,181–17,188, doi:10.1029/94JA02728.

Birn, J., A. V. Artemyev, D. N. Baker, M. Echim, M. Hoshino, and L. M. Zelenyi (2012), Particle acceleration in the magnetotail and aurora, *Space Sci. Rev.*, *179*, 49.

Boakes, P. D., S. E. Milan, G. A. Abel, M. P. Freeman, G. Chisham, and B. Hubert (2011), A superposed epoch investigation of the relation between magnetospheric solar wind driving and substorm dynamics with geosynchronous particle injection signatures, *J. Geophys. Res.*, *116*, A01214, doi:10.1029/2010JA016007.

Borovsky, J. E. (2008), The flux-tube texture of the solar wind: Strands of the magnetic carpet at 1 AU?, *J. Geophys. Res.*, *113*, A08110, doi:10.1029/2007JA012684.

Borovsky, J. E. (2010a), On the variations of the solar-wind magnetic field about the Parker spiral direction, *J. Geophys. Res.*, *115*, A09101, doi:10.1029/2009JA015040.

Borovsky, J. E. (2010b), On the contribution of strong discontinuities to the power spectrum of the solar wind, *Phys. Rev. Lett.*, *105*, 111102, doi:10.1103/PhysRevLett.105.111102.

Borovsky, J. E. (2012), The effect of sudden wind shear on the Earth's magnetosphere: Statistics of wind-shear events and CCMC simulations of magnetotail disconnections, *J. Geophys. Res.*, *117*, A06224, doi:10.1029/2012JA017623.

Borovsky, J. E., and T. E. Cayton (2011), Entropy mapping of the outer electron radiation belt between the magnetotail and geosynchronous orbit, *J. Geophys. Res.*, *116*, A06216, doi:10.1029/2011JA016470.

Borovsky, J. E., and M. H. Denton (2009a), Electron loss rates from the outer electron radiation belt caused by the filling of the outer plasmasphere: The calm before the storm, *J. Geophys. Res.*, *114*, A11203, doi:10.1029/2009JA014063.

Borovsky, J. E., and M. H. Denton (2009b), Relativistic-electron dropouts and recovery: A superposed-epoch study of the magnetosphere and the solar wind, *J. Geophys. Res.*, *114*, A02201, doi:10.1029/2008JA013128.

Borovsky, J. E., and M. H. Denton (2010a), On the heating of the outer radiation belt to produce high fluxes of relativistic electrons: Measured heating rates for high-speed stream-driven storms, *J. Geophys. Res.*, *115,* A12206, doi:10.1029/2010JA015342.
Borovsky, J. E., and M. H. Denton (2010b), The magnetic field at geosynchronous orbit during high-speed stream-driven storms: Connections to the solar wind, the plasma sheet, and the outer electron radiation belt, *J. Geophys. Res.*, *115,* A08217, doi:10.1029/2009JA015116.
Borovsky, J. E., and M. H. Denton (2010c), Solar-wind turbulence and shear: A superposed-epoch analysis of corotating interaction regions at 1 AU, *J. Geophys. Res.*, *115*, A10101, doi:10.1029/2009JA014966.
Borovsky, J. E., and M. H. Denton (2011a), A survey of the anisotropy of the outer electron radiation belt during high-speed-stream-driven storms, *J. Geophys. Res.*, *116*, A05201, doi:10.1029/2010JA016151.
Borovsky, J. E., and M. H. Denton (2011b), Evolution of the magnetotail energetic-electron population during high-speed-stream-driven storms: Evidence for the leakage of the outer electron radiation belt into the Earth's magnetotail, *J. Geophys. Res.*, *116*, A12228, doi:10.1029/2011JA016713.
Borovsky, J. E., and M. H. Denton (2013), The differences between storms driven by helmet-streamer CIRs and storms driven by pseudostreamer CIRs, *J. Geophys. Res. Space Physics*, *118*, 5506–5521, doi:10.1002/jgra.50524.
Borovsky, J. E., and M. H. Denton (2014), Exploring the cross-correlations and autocorrelations of the ULF indices and incorporating the ULF indices into the systems science of the solar-wind-driven magnetosphere, *J. Geophys. Res. Space Physics*, *119*, 4307–4334, doi:10.1002/2014JA019876.
Borovsky, J. E., and J. T. Steinberg (2006), The "calm before the storm" in CIR/magnetosphere interactions: Occurrence statistics, solar-wind statistics, and magnetospheric preconditioning, *J. Geophys. Res.*, *111,* A07S10, doi:10.1029/2005JA011397.
Borovsky, J. E., M. F. Thomsen, and D. J. McComas (1997), The superdense plasma sheet: Plasmaspheric origin, solar wind origin, or ionospheric origin?, *J. Geophys. Res.*, *102*, 22,089–22,097, doi:10.1029/96JA02469.
Borovsky, J. E., M. F. Thomsen, D. J. McComas, T. E. Cayton, and D. J. Knipp (1998a), Magnetospheric dynamics and mass flow during the November 1993 storm, *J. Geophys. Res.*, *103*, 26,373–26,394, doi:10.1029/97JA03051.
Borovsky, J. E., M. F. Thomsen, R. C. Elphic, T. E. Cayton, and D. J. McComas (1998b), The transport of plasma sheet material from the distant tail to geosynchronous orbit, *J. Geophys. Res.*, *103*, 20,297–20,331, doi:10.1029/97JA03144.
Borovsky, J. E., R. H. W. Friedel, and M. H. Denton (2014), Statistically measuring the amount of pitch angle scattering that energetic electrons undergo as they drift across the plasmaspheric drainage plume at geosynchronous orbit, *J. Geophys. Res. Space Physics*, *119*, 1814–1826, doi:10.1002/2013JA019310.
Borrini, G., J. T. Gosling, S. J. Bame, W. C. Feldman, and J. M. Wilcox (1981), Solar wind helium and hydrogen structure near the heliospheric current sheet: A signal of coronal streamers at 1 AU, *J. Geophys. Res.*, *86*, 4565–4573, doi:10.1029/JA086iA06p04565.
Boscher, D., S. Bourdarie, R. Friedel, and A. Korth (1998), Long term dynamic radiation belt model for low energy protons, *Geophys. Res. Lett.*, *25*, 4129–4132, doi:10.1029/1998GL900077.
Bourdarie, S., D. Boscher, T. Beutier, J.-A. Sauvaud, and M. Blanc (1997), Electron and proton radiation belt dynamic simulations during storm periods: A new asymmetric convection-diffusion model, *J. Geophys. Res.*, *102*, 17,541–17,552, doi:10.1029/97JA01305.
Bruno, R., V. Carbone, P. Veltri, E. Pietropaolo, and B. Bavassano (2001), Identifying intermittency events in the solar wind, *Planet. Space Sci.*, *49*, 1201, doi:10.1016/S0032-0633(01)00061-7.
Burlaga, L., E. Sittler, F. Mariani, and R. Schwenn (1981), Magnetic loop behind an interplanetary shock: Voyager, Helios, and IMP 8 observations, *J. Geophys. Res.*, *86*, 6673–6684, doi:10.1029/JA086iA08p06673.
Cayton, T. E. (2007), Trapped population of ~1 Me protons at geostationary orbit, *Rep. LA-UR-07-7169*, Los Alamos Natl. Lab., Los Alamos.
Cayton, T. E., and R. D. Belian (2007), Numerical modeling of the synchronous orbit particle analyzer (SOPA, Version 2) that flew on S/C 1990-095, *LA Rep. LA-14335*, Los Alamos Natl. Lab., Los Alamos, N. M.
Cayton, T. E., R. D. Belian, S. P. Gary, T. A. Fritz, and D. N. Baker (1989), Energetic electron components at geosynchronous orbit, *Geophys. Res. Lett.*, *16*, 147–150, doi:10.1029/GL016i002p00147.
Cornwall, J. M. (1972), Radial diffusion of ionized helium and protons: A probe for magnetospheric dynamics, *J. Geophys. Res.*, *77*, 1756–1770, doi:10.1029/JA077i010p01756.
Cornwall, J. M., F. V. Coroniti, and R. M. Thorne (1970), Turbulent loss of ring current protons, *J. Geophys. Res.*, *75*, 4699–4709, doi:10.1029/JA075i025p04699.
Crooker, N. U., and J. T. Gosling (1999), CIR morphology, turbulence, discontinuities, and energetic particles, *Space Sci. Rev.*, *89*, 179, doi:10.1023/A:1005253526438.
Crooker, N. U., S. K. Antiochos, X. Zhao, and M. Neugebauer (2012), Global network of slow solar wind, *J. Geophys. Res.*, *117*, A04104, doi:10.1029/2011JA017236.
Davis, L. R., and J. M. Williamson (1963), Low-energy trapped protons, in *Space Research: Proceedings of the Third International Conference on Space Research*, vol. 3, 365 pp., North-Holland Co., Amsterdam.
Davis, L. R., and J. M. Williamson (1966), Outer zone protons, in *Radiation Trapped in the Earth's Magnetic Field*, edited by B. McCormac, pp. 215–230, D. Reidel, Dordrecht, Netherlands.
Denton, M. H., and J. E. Borovsky (2008), Superposed epoch analysis of high-speed-stream effects at geosynchronous orbit: Hot plasma, cold plasma, and the solar wind, *J. Geophys. Res.*, *113*, A07216, doi:10.1029/2007JA012998.
Denton, M. H., and J. E. Borovsky (2009), The superdense plasma sheet in the magnetosphere during high-speed-steam-driven storms: Plasma transport timescales, *J. Atmos. Sol. Terr. Phys.*, *71*, 1045, doi:10.1016/j.jastp.2008.04.023.
Denton, M. H., and J. E. Borovsky (2012), Magnetosphere response to high-speed solar wind streams: A comparison of weak and strong driving and the importance of extended periods of fast solar wind, *J. Geophys. Res.*, *117*, A00L05, doi:10.1029/2011JA017124.
Denton, M. H., J. E. Borovsky, and T. E. Cayton (2010), A density-temperature description of the outer electron radiation belt during geomagnetic storms, *J. Geophys. Res.*, *115*, A01208, doi:10.1029/2009JA014183.
Desorgher, L., E. Fluckiger, P. Buhler, and A. Zehnder (2000), Modelling of the outer electron belt flux dropout and losses during magnetic storm main phase, *Adv. Space Res.*, *26*, 167, doi:10.1016/S0273-1177(99)01044-3.
Ebihara, Y., M.-C. Fok, J. B. Blake, and J. F. Fennell (2008), Magnetic coupling of the ring current and the radiation belt, *J. Geophys. Res.*, *113,* A07221, doi:10.1029/2008JA013267.
Falthammar, C.-G. (1973), Motion of charged particles in the magnetosphere, in *Cosmical Geophysics*, edited by A. Egeland, O. Holter, and A. Omholt, 121 pp., Universitetsforlaget, Oslo.
Fisk, L. A., and M. A. Lee (1980), Shock acceleration of energetic particles in corotating interaction regions in the solar wind, *Astrophys. J.*, *237*, 620, doi:10.1086/157907.
Forster, D. R., M. H. Denton, M. Grande, and C. H. Perry (2013), Inner magnetospheric heavy ion composition during high-speed stream-driven storms, *J. Geophys. Res. Space Physics*, *118*, 4066–4079, doi:10.1002/jgra.50292.

Foullon, C., et al. (2011), Plasmoid releases in the heliospheric current sheet and associated coronal hole boundary layer evolution, *Astrophys. J.*, *737*, 1, doi:10.1088/0004-637X/737/1/16.
Fraser, B. J., and T. S. Nguyen (2001), Is the plasmapause a preferred source region of electromagnetic ion cyclotron waves in the magnetosphere? *J. Atmos. Sol. Terr. Phys.*, *63*, 1225, doi:10.1016/S1364-6826(00)00225-X.
Freeman, J. W. (1964), The morphology of the electron distribution in the outer radiation zone and near the magnetospheric boundary as observed by Explorer 12, *J. Geophys. Res.*, *69*, 1691–1723, doi:10.1029/JZ069i009p01691.
Friedel, R. H. W., G. D. Reeves, and T. Obara (2002), Relativistic electron dynamics in the inner magnetosphere—A review, *J. Atmos. Sol. Terr. Phys.*, *64*, 265, doi:10.1016/S1364-6826(01)00088-8.
Fritz, T. A., and W. N. Spjeldvik (1979), Simultaneous quiet time observations of energetic radiation belt protons and helium ions: The equatorial α/p ratio near 1 MeV, *J. Geophys. Res.*, *84*, 2608–2618, doi:10.1029/JA084iA06p02608.
Gosling, J. T., V. Pizzo, and S. J. Bame (1973), Anomalously low proton temperatures in the solar wind following interplanetary shock waves—Evidence for magnetic bottles, *J. Geophys. Res.*, *78*, 2001–2009, doi:10.1029/JA078i013p02001.
Gosling, J. T., J. R. Asbridge, S. J. Bame, and W. C. Feldman (1978), Solar wind stream interfaces, *J. Geophys. Res.*, *83*, 1401–1412, doi:10.1029/JA083iA04p01401.
Gosling, J. T., G. Borrini, J. R. Asbridge, S. J. Bame, W. C. Feldman, and R. T. Hansen (1981), Coronal streamers in the solar wind at 1 AU, *J. Geophys. Res.*, *86*, 5438–5448, doi:10.1029/JA086iA07p05438.
Green, J. C., T. G. Onsager, T. P. O'Brien, and D. N. Baker (2004), Testing loss mechanisms capable of rapidly depleting relativistic electron flux in the Earth's outer radiation belt, *J. Geophys. Res.*, *109,* A12211, doi:10.1029/2004JA010579.
Gussenhoven, M. S., D. A. Hardy, and N. Heinemann (1983), Systematics of the equatorward diffuse auroral boundary, *J. Geophys. Res.*, *88*, 5692–5708, doi:10.1029/JA088iA07p05692.
Higbie, P. R., R. D. Belian, and D. N. Baker (1978), High-resolution energetic particle measurements at 6.6 RE 1. Electron micropulsations, *J. Geophys. Res.*, *83*, 4851–4855.
Ingraham, J. C., T. E. Cayton, R. D. Belian, R. A. Christensen, R. H. W. Friedel, M. M. Meier, G. D. Reeves, and M. Tuszewski (2001), Substorm injection of relativistic electrons to geosynchronous orbit during the great magnetic storm of March 24, 1991, *J. Geophys. Res.*, *106*, 25,759–25,776, doi:10.1029/2000JA000458.
Intrilligator, D. S., and G. L. Siscoe (1994), Stream interfaces and energetic ions closer than expected: Analyses of Pioneers 10 and 11 observations, *Geophys. Res. Lett.*, *21*, 1117–1120, doi:10.1029/94GL01071.
Jordanova, V. K. (2012), The role of the Earth's ring current in radiation belt dynamics, in *Dynamics of the Earth's Radiation Belts and Inner Magnetosphere*, *Geophys. Monog. Ser.*, vol. 199, pp. 303–314 , AGU, Washington, D. C.
Jordanova, V. K., Y. S. Miyoshi, S. Zaharia, M. F. Thomsen, G. D. Reeves, D. S. Evans, C. G. Mouikis, and J. F. Fennell (2006), Kinetic simulations of ring current evolution during the Geospace Environment Modeling challenge events, *J. Geophys. Res.*, *111*, A11S10, doi:10.1029/2006JA011644.
Kataoka, R., and Y. Miyoshi (2006), Flux enhancement of radiation belt electrons during geomagnetic storms driven by coronal mass ejections and corotating interaction regions, *Space Weather*, *4*, S09004, doi:10.1029/2005SW000211.
Kilpua, E. K. J., H. Hietala, D. L. Turner, H. E. J. Koskinen, T. I. Pulkkinen, J. V. Rodriguez, G. D. Reeves, S. G. Claudepierre, and H. E. Spence (2015), Unraveling the drivers of the storm time radiation belt response, *Geophys. Res. Lett.*, *42*, 3076–3084, doi:10.1002/2015GL063542.
Kim, K. C., D.-Y. Lee, H.-J. Kim, L. R. Lyons, E. S. Lee, M. K. Ozturk, and C. R. Choi (2008), Numerical calculations of relativistic electron drift loss effect, *J. Geophys. Res.*, *113*, A09212, doi:10.1029/2007JA013011.
King, J. H., and N. E. Papitashvili (2005), Solar wind spatial scales in and comparisons of hourly Wind and ACE plasma and magnetic field data, *J. Geophys. Res.*, *110*, A02104, doi:10.1029/2004JA010649.
Kozyra, J. U., C. E. Rasmussen, R. H. Miller, and L. R. Lyons (1994), Interaction of ring current and radiation belt protons with ducted plasmaspheric hiss: 1. Diffusion coefficients and timescales, *J. Geophys. Res.*, *99*, 4069–4084.
Kurt, V., A. Belov, H. Mavromichalaki, and M. Gerontidou (2004), Statistical analysis of solar proton events, *Ann. Geophys.*, *22*, 2255, doi:10.5194/angeo-22-2255-2004.
Lam, H.-L. (2004), On the prediction of relativistic electron fluence based on its relationship with geomagnetic activity over a solar cycle, *J. Atmos. Sol. Terr. Phys.*, *66*, 1703, doi:10.1016/j.jastp.2004.08.002.
Lanzerotti, L. J., D. C. Webb, and C. W. Arthur (1978), Geomagnetic field fluctuations at synchronous orbit 2. Radial diffusion, *J. Geophys. Res.*, *83*, 3866–3870.
Lazutin, L. L., S. N. Kuznetsov, and A. N. Podorolskii (2007), Dynamics of the radiation belt formed by solar protons during magnetic storms, *Geomagn. Aeron.*, *47*, 175, doi:10.1134/S0016793207020053.
Lazutin, L. L., Y. I. Logachev, E. A. Muravieva, and V. L. Petrov (2012), Relaxation of electron and proton radiation belts of the Earth after strong magnetic storms, *Cosmic Res.*, *50*, 1, doi:10.1134/S0010952511060062.
Liemohn, H. (1961), The lifetime of radiation belt protons with energies between 1 keV and 1 MeV, *J. Geophys. Res.*, *66*, 3593–3595, doi:10.1029/JZ066i010p03593.
Liu, Y. (2007), Halo coronal mass ejections and configuration of the ambient magnetic fields, *Astrophys. J.*, *654*, L171, doi:10.1086/511385.
McDonald, F. B., B. J. Teegarden, J. H. Trainor, T. T. von Rosenvinge, and W. R. Webber (1975), The interplanetary acceleration of energetic nucleons, *Astrophys. J.*, *203*, L149, doi:10.1086/182040.
McGuire, R. E., T. T. von Rosenvinge, and F. B. McDonald (1986), The composition of solar energetic particles, *Astrophys. J.*, *301*, 938, doi:10.1086/163958.
McPherron, R. L., D. N. Baker, and N. U. Crooker (2009), Role of the Russell-McPherron effect in the acceleration of relativistic electrons, *J. Atmos. Sol. Terr. Phys.*, *71*, 1032, doi:10.1016/j.jastp.2008.11.002.
Meredith, N. P., R. B. Horne, R. H. A. Iles, R. M. Thorne, D. Heynderickx, and R. R. Anderson (2002), Outer zone relativistic electron acceleration associated with substorm-enhanced whistler mode chorus, *J. Geophys. Res.*, *107*(A7), 1144, doi:10.1029/2001JA900146.
Meredith, N. P., R. M. Thorne, R. B. Horne, D. Summers, B. J. Fraser, and R. R. Anderson (2003), Statistical analysis of relativistic electron energies for cyclotron resonance with EMIC waves observed on CRRES, *J. Geophys. Res., 108*(A6), 1250, doi:10.1029/2002JA009700.
Mewaldt, R. A., E. C. Stone, and R. E. Vogt (1979), Characteristics of the spectra of protons and alpha particles in recurrent events at 1 AU, *Geophys. Res. Lett.*, *6*, 589–592, doi:10.1029/GL006i007p00589.
Miyoshi, Y., and R. Kataoka (2005), Ring current ions and radiation belt electrons during geomagnetic storms driven by coronal mass ejections and corotating interaction regions, *Geophys. Res. Lett.*, *32*, L21105, doi:10.1029/2005GL024590.
Morley, S. K., and M. P. Freeman (2007), On the association between northward turnings on the interplanetary magnetic field and substorm onsets, *Geophys. Res. Lett.*, *34*, L08104, doi:10.1029/2006GL028891.

Morley, S. K., R. H. W. Friedel, E. L. Spanswick, G. D. Reeves, J. T. Steinberg, J. Koller, T. Cayton, and E. Noveroske (2010), Dropouts of the outer electron radiation belt in response to solar wind stream interfaces: Global positioning system observations, *Proc. R. Soc. A*, *466*, 3329, doi:10.1098/rspa.2010.0078.

Nagai, T. (1988), "Space weather forecast" prediction of relativistic electron intensity at synchronous orbit, *Geophys. Res. Lett.*, *15*, 425–428, doi:10.1029/GL015i005p00425.

Nakada, M. P., and G. D. Mead (1965), Diffusion of protons in the outer radiation belt, *J. Geophys. Res.*, *70*, 4777–4791, doi:10.1029/JZ070i019p04777.

Nakada, M. P., J. W. Dungey, and W. N. Hess (1965), On the origin of outer-belt protons, 1, *J. Geophys. Res.*, *70*, 3529–3532, doi:10.1029/JZ070i015p03529.

Newell, P. T., T. Sotirelis, K. Liou, C.-I. Meng, and F. J. Rich (2007), A nearly universal solar wind-magnetosphere coupling function inferred from 10 magnetospheric state variables, *J. Geophys. Res.*, *112,* A01206, doi:10.1029/2006JA012015.

Onsager, T. G., G. Rostoker, H.-J. Kim, G. D. Reeves, T. Obara, H. J. Singer, and C. Smithtro (2002), Radiation belt electron flux dropouts: Local time, radial, and particle-energy dependence, *J. Geophys. Res., 107*(A11), 1382, doi:10.1029/2001JA000187.

Onsager, T. G., J. C. Green, G. D. Reeves, and H. J. Singer (2007), Solar wind and magnetospheric conditions leading to the abrupt loss of outer radiation belt electrons, *J. Geophys. Res.*, *112*, A01202, doi:10.1029/2006JA011708.

Ozeke, L. G., I. R. Mann, K. R. Murphy, I. J. Rae, D. K. Milling, S. R. Elkington, A. A. Chan, and H. J. Singer (2012), ULF wave derived radiation belt radial diffusion coefficients, *J. Geophys. Res.*, *117*, A04222, doi:10.1029/2011JA017463.

Ozeke, L. G., I. R. Mann, D. L. Turner, K. R. Murphy, A. W. Degeling, I. J. Rae, and D. K. Milling (2014), Modeling cross L shell impacts of magnetopause shadowing and ULF radial diffusion in the Van Allen belts, *Geophys. Res. Lett.*, *41*, 6556–6562, doi:10.1002/2014GL060787.

Palmer, I. D., and J. T. Gosling (1978), Shock-associated proton events at large heliocentric distances, *J. Geophys. Res.*, *83*, 2037–2046, doi:10.1029/JA083iA05p02037.

Panasyuk, M. (2004), The ion radiation belts: Experiments and models, in *Effects of Space Weather on Technology Infrastructure*, edited by I. A. Daglis, 65 pp., Kluwer Acad., Dordrecht, Netherlands.

Paularena, I. I., and J. H. King (1999), NASA's IMP 8 spacecraft, in *Interball in the ISTP Program*, edited by D. G. Sibeck and K. Kudela, 145 pp., Kluwer Acad., Dordrecht, Netherlands.

Paulikas, G. A., and J. B. Blake (1976), Modulation of trapped energetic electrons at 6.6 R_e by the interplanetary magnetic field, *Geophys. Res. Lett.*, *3*, 277–280, doi:10.1029/GL003i005p00277.

Pierrard, V., and J. Lemaire (1996), Fitting the AE-8 energy spectra with two Maxwellian functions, *Radiat. Meas.*, *26*, 333–337, doi:10.1016/1350-4487(96)00057-1.

Reames, D. V., H. V. Cane, and T. T. von Rosenvinge (1990), Energetic particle abundances in solar electron events, *Astrophys. J.*, *357*, 259, doi:10.1086/168912.

Reames, D. V., I. G. Richardson, and L. M. Barbier (1991), On the differences in element abundances of energetic ions from corotating events and from large solar events, *Astrophys. J.*, *382*, L46, doi:10.1086/186209.

Richardson, I. G. (2004), Energetic particles and corotating interaction regions in the solar wind, *Space Sci. Rev.*, *111*, 267, doi:10.1023/B:SPAC.0000032689.52830.3e.

Richardson, I. G., E. W. Cliver, and H. V. Cane (2001), Sources of geomagnetic storms for solar minimum and maximum conditions during 1972–2000, *Geophys. Res. Lett.*, *28*, 2569–2572, doi:10.1029/2001GL013052.

Richter, A. K., and A. H. Luttrell (1986), Superposed epoch analysis of corotating interaction regions at 0.3 and 1.0 AU: A comparative study, *J. Geophys. Res.*, *91*, 5873–5878.

Roederer, J. G. (1967), On the adiabatic motion of energetic particles in a model magnetosphere, *J. Geophys. Res.*, *72*, 981–992, doi:10.1029/JZ072i003p00981.

Schultz, M., and L. J. Lanzerotti (1974), *Particle Diffusion in the Radiation Belts*, Spring, New York.

Selesnick, R. S. (2006), Source and loss rates of radiation belt relativistic electrons during magnetic storms, *J. Geophys. Res.*, *111*, A04210, doi:10.1029/2005JA011473.

Sergeev, V. A., S. A. Charnyaeva, S. V. Apatenkov, N. Y. Ganushkina, and S. V. Dubyagin (2015), Energy-latitude dispersion patterns near the isotropy boundaries of energetic protons, *Ann. Geophys.*, *33*, 1059, doi:10.5194/angeo-33-1059-2015.

Sheldon, R. B. (1994), Ion transport and loss in the Earth's quiet ring current 2. Diffusion and magnetosphere-ionosphere coupling, *J. Geophys. Res.*, *99*, 5705–5720, doi:10.1029/93JA02769.

Shoji, M., and Y. Omura (2012), Precipitation of highly energetic protons by helium branch electromagnetic ion cyclotron triggered emissions, *J. Geophys. Res.*, *117*, A12210, doi:10.1029/2012JA017933.

Shprits, Y. Y., R. M. Thorne, R. Friedel, G. D. Reeves, J. Fennell, D. N. Baker, and S. G. Kanekal (2006), Outward radial diffusion driven by losses at magnetopause, *J. Geophys. Res.*, *111*, A11214, doi:10.1029/2006JA011657.

Siscoe, G. L., B. Goldstein, and A. J. Lazarus (1969), An east-eest asymmetry in the solar wind velocity, *J. Geophys. Res.*, *74*, 1759–1762, doi:10.1029/JA074i007p01759.

Smolin, S. V. (2010), Effect of magnetospheric convection on the energy distribution of protons from the Earth radiation belts, *Geomagn. Aeron.*, *50*, 298, doi:10.1134/S0016793210030035.

Smolin, S. V. (2012), Three-dimensional dynamics of the Earth's radiation belt protons during the magnetic storm, *J. Sib. Fed. Univ. Math. Phys.*, *7*, 124.

Søraas, F., K. Aarsnes, J. A. Lundblad, and D. S. Evans (1999), Enhanced pitch angle scattering of protons at mid-latitudes during geomagnetic storms, *Phys. Chem. Earth C*, *24*, 287.

Spjeldvik, W. N. (1977), Equilibrium structure of equatorially mirroring radiation belt protons, *J. Geophys. Res.*, *82*, 2801–2808, doi:10.1029/JA082i019p02801.

Stevens, J. R., E. F. Martina, and R. Stephen White (1970), Proton energy distributions from 0.060 to 3.3 MeV at 6.6 Earth radii, *J. Geophys. Res.*, *75*, 5373–5385.

Suess, S. T., Y.-K. Ko, R. Von Steiger, and R. L. Moore (2009), Quiescent current sheets in the solar wind and origins of slow wind, *J. Geophys. Res.*, *114*, A04103, doi:10.1029/2008JA013704.

Summers, D., C. Ma, N. P. Meredith, R. B. Horne, R. M. Thorne, and R. R. Anderson (2004), Modeling outer-zone relativistic electron response to whistler-mode chorus activity during substorms, *J. Atmos. Sol. Terr. Phys.*, *66*, 133, doi:10.1016/j.jastp.2003.09.013.

Tanskanen, E. I., A. Viljanen, T. I. Pulkkinen, R. Prjola, L. Hakkinen, A. Pulkkinen, and O. Amm (2001), At substorm onset, 40% of AL comes from underground, *J. Geophys. Res.*, *106*, 13,119–13,134, doi:10.1029/2000JA900135.

Thomsen, M. F. (2004), Why *Kp* is such a good measure of magnetospheric convection, *Space Weather*, *2*, S11044, doi:10.1029/2004SW000089.

Thomsen, M. F., M. H. Denton, V. K. Jordanova, L. Chen, and R. M. Thorne (2011), Free energy to drive equatorial magnetosonic wave instability at geosynchronous orbit, *J. Geophys. Res.*, *116*, A08220, doi:10.1029/2011JA016644.

Thorne, R. M., R. B. Horne, V. K. Jordanova, J. Bortnik, and S. Glauert (2006), Interaction of EMIC waves with thermal plasma and radiation belt particles, in *Magnetospheric ULF Waves*, edited by K. Takahashi et al., 213 pp., AGU, Washington, D. C.

Tsurutani, B. T., C. M. Ho, E. J. Smith, M. Neugebauer, B. E. Goldstein, J. S. Mok, J. K. Arballo, A. Balogh, D. J. Southwood, and W. C. Feldman (1994), The relationship between interplanetary discontinuities and Alfven waves: Ulysses observations, *Geophys. Res. Lett.*, *21*, 2267–2270, doi:10.1029/94GL02194.

Tsyganenko, N. A. (1982), Pitch-angle scattering of energetic particles in the current sheet of the magnetospheric tail and stationary distribution functions, *Planet. Space Sci.*, *30*, 433, doi:10.1016/0032-0633(82)90052-6.

Turner, D. L., Y. Shprits, M. Hartinger, and V. Angelopoulos (2012), Explaining sudden loss of outer radiation belt electrons during geomagnetic storms, *Nat. Phys.*, *8*, 208, doi:10.1038/nphys2185.

Turner, D. L., et al. (2014), On the cause and extent of outer radiation belt losses during the 30 September 2012 dropout event, *J. Geophys. Res. Space Physics*, *119*, 1530–1540, doi:10.1002/2013JA019446.

Tverskaya, L. V., et al. (2008), Solar proton increases and dynamics of the electron outer radiation belt during solar events in December 2006, *Geomagn. Aeron.*, *48*, 719, doi:10.1134/S0016793208060042.

Ukhorskiy, A. Y., B. J. Anderson, P. C. Brandt, and N. A. Tsyganenko (2006), Storm time evolution of the outer radiation belt: Transport and losses, *J. Geophys. Res.*, *111*, A11S03, doi:10.1029/2006JA011690.

Ukhorskiy, A. Y., Y. Y. Shprits, B. J. Anderson, K. Takahashi, and R. M. Thorne (2010), Rapid scattering of radiation belt electrons by storm-time EMIC waves, *Geophys. Res. Lett.*, *37*, L09101, doi:10.1029/2010GL042906.

Vacaresse, A., D. Boscher, S. Bourdarie, M. Blanc, and J. A. Sauvaud (1999), Modeling the high-energy proton belt, *J. Geophys. Res.*, *104*, 28,601–28,613, doi:10.1029/1999JA900411.

Villalon, E., and W. J. Burke (1994), Diffusion of radiation belt protons by whistler waves, *J. Geophys. Res.*, *99*, 21,329–21,340, doi:10.1029/94JA01480.

Walt, M., H. D. Voss, S. J. Lev-Tov, J. Bobilia, and J.-M. Jahn (2001), Diffusion of 155 to 430 keV protons in the Earth's radiation belt, *J. Geophys. Res.*, *106*, 5957–5966, doi:10.1029/2000JA003029.

Wang, Y.-M., N. R. Sheeley, D. G. Socker, R. A. Howard, and N. B. Rich (2000), The dynamical nature of coronal streamers, *J. Geophys. Res.*, *105*, 25,113–25,142, doi:10.1029/2000JA000435.

Weygand, J. M., R. L. McPherron, K. Kauristie, H. U. Frey, and T.-S. Hsu (2008), Relation of auroral substorm onset to local AL index and dispersionless particle injections, *J. Atmos. Sol. Terr. Phys.*, *70*, 2336, doi:10.1016/j.jastp.2008.09.030.

Xu, F., and J. E. Borovsky (2015), A new 4-plasma categorization scheme for the solar wind, *J. Geophys. Res. Space Physics*, *120*, 70–100, doi:10.1002/2014JA020412.

Yershkovitch, A. I., V. P. Shabansky, and A. E. Antonova (1965), Hypothesis of origin and formation of radiation belts as a result of particle drift into the depth of the magnetosphere, in *Proceedings of the 9th International Conference on Cosmic Rays*, vol. 1, 543 pp., London.

Yu, Y., J. Koller, and S. K. Morley (2013), Quantifying the effect of magnetopause shadowing on electron radiation belt dropouts, *Ann. Geophys.*, *31*, 1929, doi:10.5194/angeo-31-1929-2013.